Nuclear Fragmentation Cross Section Modeling for Space Radiation Applications

A Dissertation Presented for the

Doctor of Philosophy

Degree

The University of Tennessee, Knoxville

Wouter C. de Wet

December 2017

© by Wouter C. de Wet, 2017
All Rights Reserved.

For my wife, Lauren.

Abstract

One of the most significant challenges to overcome on the journey to Mars is understanding the biological risk associated with the space radiation environment. Radiation transport codes are one of the tools necessary to quantify this risk. Due to the nature of the space radiation environment, it is of great importance that these transport codes are able to describe the breakup of heavy ions into smaller fragments—light ions in particular. For this, event generators within radiation transport codes rely on nuclear fragmentation codes to predict the products of high energy nuclear collisions. This manuscript documents the development of a nuclear fragmentation code: the Relativistic Abrasion-Ablation and Deexcitation Fragmentation Model (RAADFRG). RAADFRG is the product of a collaboration between the University of Tennessee and NASA's Langley Research Center (LaRC), and is being developed for space radiation applications. Currently, total isotopic yield is of primary concern; however, future versions of the model must predict double differential isotopic yields. The collision model is a framework of smaller physics packages, each meant to describe a specific physical phenomenon within the abrasion-ablation heavy ion collision theory. The coalescence model, along with the collision framework architecture and development, are my primary original contributions.

Table of Contents

1 Introduction **1**

1.1 Background 1

1.1.1 Radiation Effects and Limits 1

1.1.2 Significance of Light Ion Production 2

1.1.3 Nuclear Collision Mechanism 3

1.2 Problem Statement 3

1.3 Objective 3

1.4 Contributions 4

1.4.1 Original 4

1.4.2 Collaborative 5

2 Review of Literature **6**

2.1 Evaporation Theory 6

2.2 Coalescence 8

3 Methodology **11**

3.1 Model Framework Overview 11

3.2 Abrasion Model 12

3.2.1 Total Abrasion Reaction Cross Section 12

3.2.2 Pre-fragment Cross Sections 12

3.2.3 Excitation Energy 13

3.3 Evaporation Model 13

3.3.1 Level Density 15

3.3.2 Pairing Energy Correction . . . 16
3.3.3 Capture Cross Section . . . 16
3.3.4 Emission Width . . . 17
3.3.5 Emission Kinetic Energy and Angle . . . 18
3.4 Coalescence Model . . . 19
3.4.1 Abraded Nucleon Cross Sections . . . 19
3.4.2 Coalesced Particle Multiplicity . . . 20
3.4.3 Coalescence Cross Sections . . . 21
3.4.4 Coalescence Radius . . . 24
3.5 Electromagnetic Dissociation . . . 25

4 Results and Conclusion **26**
4.1 Evaporation Results . . . 26
4.2 Coalescence Results . . . 29
4.3 Elemental and Isotopic Production Cross Sections . . . 34
4.4 Conclusion . . . 60

Bibliography **61**

Appendices **68**

A Relevant Tables **69**

Vita **71**

List of Tables

A.1 Tabulated parameters for calculating charged particle Coulomb barrier (k_j), and capture cross sections (c_j) Ref. [9]. See Section 3.3.3 for implementation. 70

List of Figures

4.1 Light ion production from evaporation in the reaction of ^{12}C on ^{12}C at a beam energy of 1572 MeV/A. 27

4.2 Neutron production from evaporation in the reaction of ^{12}C on ^{12}C at a beam energy of 1572 MeV/A. The vertical axis is cross section (mb), the right axis is emitted angle (degrees), and the left axis is emitted energy (MeV). 27

4.3 Proton production from evaporation in the reaction of ^{12}C on ^{12}C at a beam energy of 1572 MeV/A. The vertical axis is cross section (mb), the right axis is emitted angle (degrees), and the left axis is emitted energy (MeV). 28

4.4 Alpha production from evaporation in the reaction of ^{12}C on ^{12}C at a beam energy of 1572 MeV/A. The vertical axis is cross section (mb), the right axis is emitted angle (degrees), and the left axis is emitted energy (MeV). 28

4.5 A comparison of light ion production cross sections from RAADFRG and experimental measurements from Ref. [38] for the collision reaction: ^{12}C on ^{9}Be at 290 MeV/A. 30

4.6 A comparison of light ion production cross sections from RAADFRG and experimental measurements from Ref. [38] for the collision reaction: ^{12}C on ^{9}Be at 1050 MeV/A. 30

4.7 A comparison of light ion production cross sections from RAADFRG and experimental measurements from Ref. [38] for the collision reaction: ^{12}C on ^{64}Cu at 1050 MeV/A. 31

4.8 A comparison of light ion production cross sections from RAADFRG and experimental measurements from Ref. [38] for the collision reaction: ^{12}C on ^{12}C at 1050 MeV/A. 31

4.9 A comparison of light ion production cross sections from RAADFRG and experimental measurements from Ref. [38] for the collision reaction: ^{12}C on ^{207}Pb at 1050 MeV/A. 32
4.10 A comparison of light ion production cross sections from RAADFRG and experimental measurements from Ref. [38] for the collision reaction: ^{16}O on ^{9}Be at 2100 MeV/A. 32
4.11 A comparison of light ion production cross sections from RAADFRG and experimental measurements from Ref. [38] for the collision reaction: ^{16}O on ^{12}C at 2100 MeV/A. 33
4.12 A comparison of light ion production cross sections from RAADFRG and experimental measurements from Ref. [38] for the collision reaction: ^{16}O on ^{64}Cu at 2100 MeV/A. 33
4.13 Elemental production cross sections (solid) compared with experimental measurements (error bars) from Ref. [53] for the reaction of ^{12}C on ^{12}C at 289 MeV/A. 35
4.14 Elemental production cross sections (solid) compared with experimental measurements (error bars) from Ref. [29] for the reaction of ^{12}C on ^{12}C at 600 MeV/A. 35
4.15 Elemental production cross sections (solid) compared with experimental measurements (error bars) from Ref. [55] for the reaction of ^{16}O on ^{27}Al at 290 MeV/A. 36
4.16 Elemental production cross sections (solid) compared with experimental measurements (error bars) from Ref. [29] for the reaction of ^{20}Ne on ^{12}C at 599 MeV/A. 36
4.17 Elemental production cross sections (solid) compared with experimental measurements (error bars) from Ref. [29] for the reaction of ^{20}Ne on ^{12}C at 1057 MeV/A. 37
4.18 Elemental production cross sections (solid) compared with experimental measurements (error bars) from Ref. [55] for the reaction of ^{24}Mg on ^{12}C at 400 MeV/A. 37

4.19 Elemental production cross sections (solid) compared with experimental measurements (error bars) from Ref. [29] for the reaction of ^{27}Al on ^{12}C at 582 MeV/A. 38
4.20 Elemental production cross sections (solid) compared with experimental measurements (error bars) from Ref. [52] for the reaction of ^{28}Si on ^{208}Pb at 290 MeV/A. 38
4.21 Elemental production cross sections (solid) compared with experimental measurements (error bars) from Ref. [52] for the reaction of ^{28}Si on ^{12}C at 400 MeV/A. 39
4.22 Elemental production cross sections (solid) compared with experimental measurements (error bars) from Ref. [52] for the reaction of ^{28}Si on ^{27}Al at 400 MeV/A. 39
4.23 Elemental production cross sections (solid) compared with experimental measurements (error bars) from Ref. [52] for the reaction of ^{28}Si on ^{120}Sn at 400 MeV/A. 40
4.24 Elemental production cross sections (solid) compared with experimental measurements (error bars) from Ref. [54] for the reaction of ^{35}Cl on ^{12}C at 650 MeV/A. 40
4.25 Elemental production cross sections (solid) compared with experimental measurements (error bars) from Ref. [54] for the reaction of ^{35}Cl on ^{27}Al at 650 MeV/A. 41
4.26 Elemental production cross sections (solid) compared with experimental measurements (error bars) from Ref. [54] for the reaction of ^{35}Cl on ^{63}Cu at 650 MeV/A. 41
4.27 Elemental production cross sections (solid) compared with experimental measurements (error bars) from Ref. [54] for the reaction of ^{35}Cl on ^{120}Sn at 650 MeV/A. 42
4.28 Elemental production cross sections (solid) compared with experimental measurements (error bars) from Ref. [54] for the reaction of ^{35}Cl on ^{208}Pb at 650 MeV/A. 42

4.29 Elemental production cross sections (solid) compared with experimental measurements (error bars) from Ref. [54] for the reaction of ^{35}Cl on ^{12}C at 1000 MeV/A. 43
4.30 Elemental production cross sections (solid) compared with experimental measurements (error bars) from Ref. [54] for the reaction of ^{35}Cl on ^{27}Al at 1000 MeV/A. 43
4.31 Elemental production cross sections (solid) compared with experimental measurements (error bars) from Ref. [54] for the reaction of ^{35}Cl on ^{63}Cu at 1000 MeV/A. 44
4.32 Elemental production cross sections (solid) compared with experimental measurements (error bars) from Ref. [54] for the reaction of ^{35}Cl on ^{120}Sn at 1000 MeV/A. 44
4.33 Elemental production cross sections (solid) compared with experimental measurements (error bars) from Ref. [54] for the reaction of ^{35}Cl on ^{208}Pb at 1000 MeV/A. 45
4.34 Elemental production cross sections (solid) compared with experimental measurements (error bars) from Ref. [18] for the reaction of ^{36}Ar on ^{27}Al at 359 MeV/A. 45
4.35 Elemental production cross sections (solid) compared with experimental measurements (error bars) from Ref. [18] for the reaction of ^{36}Ar on ^{12}C at 361 MeV/A. 46
4.36 Elemental production cross sections (solid) compared with experimental measurements (error bars) from Ref. [31] for the reaction of ^{40}Ar on ^{9}Be at 90 MeV/A. 46
4.37 Elemental production cross sections (solid) compared with experimental measurements (error bars) from Ref. [47] for the reaction of ^{40}Ar on ^{12}C at 213 MeV/A. 47
4.38 Elemental production cross sections (solid) compared with experimental measurements (error bars) from Ref. [54] for the reaction of ^{40}Ar on ^{12}C at 290 MeV/A. 47

4.39 Elemental production cross sections (solid) compared with experimental measurements (error bars) from Ref. [54] for the reaction of ^{40}Ar on ^{27}Al at 290 MeV/A. 48
4.40 Elemental production cross sections (solid) compared with experimental measurements (error bars) from Ref. [54] for the reaction of ^{40}Ar on ^{63}Cu at 290 MeV/A. 48
4.41 Elemental production cross sections (solid) compared with experimental measurements (error bars) from Ref. [54] for the reaction of ^{40}Ar on ^{120}Sn at 290 MeV/A. 49
4.42 Elemental production cross sections (solid) compared with experimental measurements (error bars) from Ref. [18] for the reaction of ^{40}Ar on ^{27}Al at 359 MeV/A. 49
4.43 Elemental production cross sections (solid) compared with experimental measurements (error bars) from Ref. [18] for the reaction of ^{40}Ar on ^{12}C at 361 MeV/A. 50
4.44 Elemental production cross sections (solid) compared with experimental measurements (error bars) from Ref. [54] for the reaction of ^{40}Ar on ^{12}C at 400 MeV/A. 50
4.45 Elemental production cross sections (solid) compared with experimental measurements (error bars) from Ref. [54] for the reaction of ^{40}Ar on ^{27}Al at 400 MeV/A. 51
4.46 Elemental production cross sections (solid) compared with experimental measurements (error bars) from Ref. [29] for the reaction of ^{40}Ar on ^{12}C at 600 MeV/A. 51
4.47 Elemental production cross sections (solid) compared with experimental measurements (error bars) from Ref. [54] for the reaction of ^{40}Ar on ^{208}Pb at 650 MeV/A. 52
4.48 Elemental production cross sections (solid) compared with experimental measurements (error bars) from Ref. [48] for the reaction of ^{40}Ar on ^{12}C at 792 MeV/A. 52

4.49 Elemental production cross sections (solid) compared with experimental measurements (error bars) from Ref. [54] for the reaction of ^{48}Ti on ^{12}C at 1000 MeV/A. 53
4.50 Elemental production cross sections (solid) compared with experimental measurements (error bars) from Ref. [54] for the reaction of ^{48}Ti on ^{27}Al at 1000 MeV/A. 53
4.51 Elemental production cross sections (solid) compared with experimental measurements (error bars) from Ref. [29] for the reaction of ^{56}Fe on ^{12}C at 600 MeV/A. 54
4.52 Elemental production cross sections (solid) compared with experimental measurements (error bars) from Ref. [29] for the reaction of ^{56}Fe on ^{63}Cu at 1569 MeV/A. 54
4.53 Isotopic production cross sections (solid) compared with experimental measurements (error bars) from Ref. [29] for the reaction of ^{12}C on ^{12}C at 1050 MeV/A. 55
4.54 Isotopic production cross sections (solid) compared with experimental measurements (error bars) from Ref. [55] for the reaction of ^{16}O on ^{12}C at 290 MeV/A. 55
4.55 Isotopic production cross sections (solid) compared with experimental measurements (error bars) from Ref. [7] for the reaction of ^{36}Ar on ^{9}Be at 1050 MeV/A. 56
4.56 Isotopic production cross sections (solid) compared with experimental measurements (error bars) from Ref. [31] for the reaction of ^{40}Ar on ^{9}Be at 90 MeV/A. 57
4.57 Isotopic production cross sections (solid) compared with experimental measurements (error bars) from Ref. [47] for the reaction of ^{40}Ar on ^{12}C at 213 MeV/A. 58
4.58 Isotopic production cross sections (solid) compared with experimental measurements (error bars) from Ref. [29] for the reaction of ^{40}Ar on ^{12}C at 600 MeV/A. 59

4.59 Isotopic production cross sections (solid) compared with experimental measurements (error bars) from Ref. [29] for the reaction of ^{56}Fe on ^{12}C at 600 MeV/A. 59

Chapter 1

Introduction

1.1 Background

1.1.1 Radiation Effects and Limits

When high-energy heavy-charged (HZE) particles collide directly with atomic nuclei in shielding material or human tissue, they tend to fragment into lighter particles. Radiation transport codes use fragmentation cross sections, also referred to as production cross sections, to quantify this phenomenon. These lighter secondary particles may also undergo direct collisions of their own, fragmenting yet again. The primary radiation, and subsequent generations of particles it may produce, interact via the Coulomb force to ionize or excite molecular and atomic electrons in the matter they traverse. In the case of biological tissue, these ionizations can result in either direct DNA damage, or the production of free radicals, which in turn attack DNA sites. Misrepair of damage done to genetic material is responsible for carcinogenesis, cataract formation, and other biological consequences.

NASA has set permissible exposure limits (PELs) on astronaut career effective doses in order to mitigate the potential risks from radiation doses received by space crew during manned operations in space. The PELs have been established to adhere to the criteria that there may be no more than a 3% increase in risk at the 95% confidence interval of exposure-induced death from career exposure. Organ-specific dose limits are set independently for the eye

lens, skin, blood-forming organs, heart, and the central nervous system to protect against short-term and non-cancer effects [8].

1.1.2 Significance of Light Ion Production

While the spectra comprising the space radiation environment are well known, this information alone does not suffice to describe the biological risks associated with manned space travel. Energy deposition and the associated biological consequences depend strongly on both particle energy and isotope. Therefore, one must know the specific composition of the dose-imparting spectra in order to calculate dose and biological risk. Since radiation transport codes use cross sections to calculate these values, accurate cross sections are necessary to ensure that space crew do not exceed the NASA PELs.

In this manuscript, the term light ion is a reference to any nucleus with a mass and charge equal to or less than that of the alpha particle, including neutrons. The accuracy of light ion production cross sections is of particular importance, as these species make large contributions to dose equivalent [36]. Most transport codes are in reasonable agreement when predicting heavy ion production cross sections. There are large discrepancies, however, between the values predicted for light ion production by various radiation transport codes. Light ion production becomes complicated to predict because there are many different mechanisms within a nuclear collision in which light ions are produced. For example, the framework described in this manuscript has four separate mechanisms in which light ions are produced. These production mechanisms include the coalescence of abraded nucleons from the frictional overlap region, evaporation from an excited pre-fragment, leftover residual nuclei from evaporation, and electromagnetic dissociation from the parent nucleus. The errors associated with each of the production mechanisms compound, resulting in potentially large errors in the final light ion cross sections.

1.1.3 Nuclear Collision Mechanism

Inelastic collisions of relativistic heavy ions are modeled using a two step abrasion-ablation reaction mechanism, as well as an electromagnetic dissociation mechanism (EMD). The contributions of the two phenomena are calculated independently and summed. In other words, the inelastic reaction cross section can be described as the sum of the total abrasion and EMD cross sections. In the abrasion-ablation mechanism, a projectile nucleus strikes a stationary target nucleus with some impact parameter representing the distance between the two nuclear center points. The region of overlap between the nuclei is a function of this impact parameter and the radii of the two participant nuclei. All nucleons within the overlap region are assumed to be removed from their parent nucleus during the interaction [1]. Some of the removed nucleons coalesce to form light ions (see Section 3.4). The deformed remains of the parent nucleus, called a pre-fragment, each retain their specific momenta after the interaction and continue on to undergo ablation, also termed evaporation throughout this manuscript, as described in Chapter 3. The significant difference between their relative momenta allows for target and projectile breakup to be calculated independently within their respective rest frames. The projectile quantities are then Lorentz transformed to lab frame and combined with the results from the target breakup to form total yield cross sections.

1.2 Problem Statement

As described in Section 1.1 and discussed in detail in Ref. [26], NASA requires a nuclear fragmentation code with the ability to accurately calculate fragmentation production cross sections from nuclear collisions relevant to the space radiation environment. This is especially true if we plan to put human beings on Mars by the mid 2030's.

1.3 Objective

The primary objective of this work is to develop the Relativistic Abrasion-Ablation Deexcitation Fragmentation Code (RAADFRG). The RAADFRG package is a nuclear fragmentation model capable of accurately predicting elemental and isotopic production

cross sections for nuclear collisions of all combinations of participants, excluding single-nucleons, and energies relevant to human-factors endpoints in the extraterrestrial radiation environment. In this work, we are primarily concerned with total elemental and isotopic yields. However, the code is developed with the intention of producing double differential cross sections in the future. Model development is performed by implementing existing theory from literature, if available. When necessary, existing theory is modified using physical justification in order to better fit the needs of the fragmentation model. New formulation is derived when existing theory is missing or does not suffice to accurately model experimental results.

1.4 Contributions

This model is the result of a collaborative effort among an entire team of investigators and developers. For the sake of clarity, please refer to Section 1.4.1 to view topics that contain original contributions, and Section 1.4.2 for a list of collaborative contributions.

1.4.1 Original

Each of the topics in this section contain an original contribution within their formulation or implementation in some form. The scope of originality and the degree of the impact upon the model performance vary greatly between each topic. Therefore, a brief description of the original contributions within each respective topic is given here.

Architecture/Framework Assembly

The encompassing framework responsible for performing the collision calculation is original content. The framework takes collision inputs such as projectile nucleus identity, projectile nucleus kinetic energy, and target nucleus identity, and directs the flow of data between the relevant physics models. For more information, refer to Section 3.1.

Nuclear Level Density Pairing Correction

The form of pairing energy correction within the nuclear level density formula in this model is an original contribution. The new derivation accounts for the pairing energy of the emitted particle as well as that of the residual daughter nucleus. The pairing energy corrections for all nuclei are based upon a modified version of the liquid drop pairing energy. For more information, refer to Section 3.3.2.

Coalescence of Abraded Nucleons

The physics package implemented to model the production of light ions from abraded nucleon coalescence is an original contribution. Although it is built by expanding upon existing theory available in literature, the new derivation is unique in many ways. The coalescence phenomenon is approached using a more physical argument, and is directly coupled to the abrasion formalism. For more information, refer to Section 3.4.3.

1.4.2 Collaborative

Evaporation Code Modernization

The code used in this framework to model the deexcitation of excited pre-fragments via light ion emission is based on a code originally developed using legacy FORTRAN. The modernization and translation of the legacy evaporation code was an extensive effort performed in collaboration with William P. Ford.

Chapter 2

Review of Literature

2.1 Evaporation Theory

The second step in a nuclear collision is the evaporation cascade, commonly referred to as ablation or the 'slow' cascade in literature. The deformed remaing portion of the projectile nucleus, or pre-fragment, is left in an excited state after the abrasion process. This pre-fragment will deexcite by emitting a light ion. Weisskopf and Ewing [50] derived a formalism to describe the emission width as the integral over emission probability (Eq. 3.3). This formalism is the basis upon which nearly all nuclear evaporation models are designed today. The probability of emission is proportional to the inverse reaction (capture) cross section, the emitted particle kinetic energy, and the ratio of level densities of the residual daughter and parent nuclei. From this, one may express the branching ratios for various decay channels. This process is discussed in detail in Section 3.3. The rest of this section will focus on specific relevant differences in interpretation and implementations throughout literature.

Dostrovsky et al. [9] recommend that the level density of excited states used in calculating the emission width be that of a completely degenerate Fermi gas in which the excitation energy is shifted to account for pairing effects on the ground state energy [17]. This level density method is aptly referred to as the Back-Shifted Fermi Gas Model. The ground state energy correction in this model is related to, but not necessarily equal to, the pairing energy

of the nucleus.

The excitation energy correction is thought to be responsible for producing the odd-even sawtooth pattern observed in elemental and isotopic fragmentation cross sections. In the case of the Dostrovsky model, these corrections are unique to each nucleus and are treated as freely adjustable parameters with no attempt made at physical justification. While this model does reasonably well for reproducing specific evaporation channels, it does not reproduce the odd-even behaviour. Moller et al. [30] performed a comprehensive study of various nuclear pairing models to great extent and produced an excellent overview of the differences between the Bardeen-Cooper-Schrieffer, Lipkin-Nogami, and conventional $12/\sqrt{\mathrm{A}}$-like models. Kataria [19] proposes that the excitation energy correction in the exponent of the level density formula is indeed the pairing energy; however, the pairing energy for highly deformed nuclei differ from the conventional liquid drop values. Thus, Kataria introduces a shell and deformation-dependent nuclear level density formula. However, no comparisons with experimental fragmentation data are published for this model.

The level density is also sensitive to the level density parameter in the exponential term (see Section 3.3.1). The Dostrovsky model uses a value of A/20 MeV for the level density parameter. However most of the literature recommends using $A/8$ MeV. Behkami et al. [5] show that this parameterization is not adequate near magic nuclei. Further investigation show that this level density parameter is actually dependent on the temperature of the pre-fragment, and a thorough parameterization was produced by Shlomo and Natowitz [40] for nuclei with masses $40 \leq \mathrm{A} \leq 210$.

Lang and Couteur [24] assembled evidence for a phase transition in nuclear matter at high excitation energies. This phase transition is not considered in the Dostrovsky model. Gilbert and Cameron propose a comprehensive shell-dependent level density formula based on nuclear temperature, including the spin and mass-dependence of the level density parameter. This formalism gives two prescriptions for the nuclear level density in order to account for a phase change in nuclear parity at higher excitation energies [11]. The Gilbert-Cameron

model is widely used today, however it does not perform well for specific nuclei with A < 40 or in the proximity of magic numbers. Gaimard and Schmidt [10] use a similar approach, based on the formalism proposed by Campi and Hufner, and are able to reproduce the odd-even effect as the result of fine-structure effects in the level density below the phase transition energy.

2.2 Coalescence

Observations in light ion double differential production cross sections show an inverse power law relationship between the magnitudes of light ion and nucleon distributions for angles off of the beam angle [3, 33, 2]. Further investigation suggests that they share a common production mechanism from a source with a well defined temperature with a significant correlation to the beam energy. Thus, it is theorized that these particles are likely formed in the overlap, or 'fireball', region of the collision.

Nearly all heavy ion fragmentation models intended to calculate light ion yields employ a coalescence model of some form. Although the underlying principle is fairly straightforward, most models rely heavily upon parameterizations. Generally, coalescence models designed for collisions with energies comparable to the space radiation environment calculate the formation of light ions from nucleons participating in the collision. Coherent models have also been developed for calculating hadron production in relativistic heavy ion collisions from coalescence of soft partons in quark-gluon plasma and hard partons from minijets [14]. Generally, light ion production via coalescence is considered for fragments with mass ^{2}H up to ^{4}He. For collisions of very heavy systems, such as Au-Au, coalescence of larger composite becomes more significant. The event generators in MCNP6 allow for fragments as heavy as $A \leq 7$ for the cascade-excitation model (CEM) and $A \leq 12$ for the Los Alamos version of the quark-gluon string model (LAQGSM) [28].

Nucleons that participate directly in the abrasion collision, or in some formalisms are explicitly emitted during the intra-nuclear cascade, and that occupy some volume in

momentum space, are assumed to coalesce before thermal equilibrium, also called freeze-out, occurs. The original generalized form of the governing equation for coalescence (see Eq. 3.23) has been derived by Awes et. al [3]. In this derivation, as with most formalisms, the coalescence mechanism is modeled for both the projectile and target nuclei over all impact parameters at once. Accordingly, the abraded nucleon multiplicities are considered to be the sums of the target and parent proton and neutron numbers. This method relies on parameterizations to average over physical details.

Awes et al. [3] state that light ion emission is nearly isotropic from a rest frame moving at about half the beam energy, and that the majority of light ions are produced in central collisions. Awes et al. also report that accurate reproduction of experimental light ion spectra for O-U at 315 MeV/A required implementing a Coulomb correction in the coalescence equation. With the Coulomb correction, they were able to very reasonably reproduce experimental observations for forward scattering angles. However, Auble et al. [2] use a similar derivation, including composite particle spin and a source emission radius calculated using the thermodynamic model, and are able to very accurately parameterize experimental double differential spectra for O-Ni collisions. Gutbrot et al. [16] were able to extract coalescence radii from experimental results using the model from Ref. [3] with no Coulomb correction, and very closely fit experimental distributions for forward and back-scattering angles.

Measurements by Gosset et al. [13] show evidence for two major classes of light ion fragments measured at various angles off of the beam axis: one slow-moving source with an intermediate temperature, and another high-temperature source moving at a velocity between that of the projectile and target systems. The NUCFRG3 code was the first to separate coalescence into projectile and target contributions, but the coalescence calculation still averages over all impact parameters [1]. This model does not implement a thermodynamic consideration to calculate source emission radius, and instead relies only on the coalescence radius, projectile nucleon multiplicities, and the total proton cross section.

Beach [4] extracts coalescence radii from light ion fragmentation data for a plethora of reactions using a temperature dependent model including composite particle spin. Lemaire et al. [25] use light ion fragmentation cross section measurements for C-C, C-Pb, Ne-NaF, Ne-Pb, Ar-KCl, and Ar-Pb reactions, over a range of energies from 400 Mev/A to 2.1GeV/A, to extract coalescence radii for each reaction. These were then used to extract source emission radii for each system. PourArsalan [39] approaches the problem from the other side by calculating the source emission radius from reaction parameters, and then extracting the coalescence radius using the thermodynamic model. Kolybasov and Sokolskikh [23] take a graphical approach to describe the coalescence radius as a function of parent mass number and the slope parameter of the inclusive nucleon spectra, and have found it to be bounded to values below about 300 MeV/c, which is in good agreement with other experimental findings.

Nakai et al. [34] measured light ion production cross sections from proton induced target breakup for a variety of targets at a beam energy of 12 GeV. Measurements were made at an angle perpendicular to the beam direction. Using a simple coalescence model, including composite particle spin, Nakai et al. are able to obtain excellent agreement with the experimental measurements.

Chapter 3

Methodology

3.1 Model Framework Overview

RAADFRG is built in modern Fortran, and has a modular structure in order to simplify the process of modifying or replacing specific physics packages within the code. The collision module drives the workflow of mechanisms. To begin, it creates all necessary input files and calls the abrasion module to calculate pre-fragment cross sections. The abrasion code also calls the excitation energy module during execution and outputs an excitation energy for each pre-fragment, along with its corresponding abrasion cross section, back to the collision module. The collision model then renormalizes these pre-fragment cross sections if an option to do so is selected, before independently calling the coalescence, evaporation, and electromagnetic dissociation modules. The three aforementioned modules return their respective results to the collision module, which consolidates the output of each to isotopic fragmentation cross sections. In the case of the projectile, these cross sections are transformed to the laboratory frame. The entire workflow is then executed again for the target nucleus, and the outputs are combined with the transformed contributions from the projectile nucleus to give the final fragmentation cross sections.

3.2 Abrasion Model

The inelastic reaction cross section, excluding contributions from the electromagnetic dissociation mechanism (see Section 3.5), is considered to be the sum of discrete abrasion reaction channels (Eq. 3.20). The abrasion module is responsible for calculating the abrasion reaction cross section and distributing it across a set of discrete abrasion channels. In each abrasion channel, i, some number of nucleons are removed from the projectile, leaving behind a deformed pre-fragment with some excitation energy. This section summarizes how these cross sections and excitation energies are calculated.

3.2.1 Total Abrasion Reaction Cross Section

This section is not covered in this dissertation. The code and formalism for this mechanism are the work of Charles M. Werneth from NASA Langley Research Center. RAADFRG currently uses the eikonal approximation to calculate the differential abrasion cross section, and then integrates to get total abrasion cross section. There are options in the code to normalize the cross sections using Tripathi's reaction cross section parameterizations [44], as well the standard eikonal abrasion model.

3.2.2 Pre-fragment Cross Sections

Pre-fragment cross sections, $\sigma^i_{\rm abr}(\mathrm{Z}_{\mathrm{PF}^i}, \mathrm{A}_{\mathrm{PF}^i})$, are calculated using the optical model described in Ref. [42]. The abrasion reaction cross sections are then distributed according to their number of frictional spectator interactions in Eq. 3.1 [41]. Below, $n^i_q \in [0, ..(d\mathrm{n}^i + d\mathrm{z}^i)]$ is the number of struck nucleons scattered into a pre-fragment (see Section 3.4.1) by

$$\sigma^i_{\rm abr}(\mathrm{Z}_{\mathrm{PF}^i}, \mathrm{A}_{\mathrm{PF}^i}, n^i_q) = \left(\begin{array}{c} d\mathrm{n}^i + d\mathrm{z}^i \\ n^i_q \end{array} \right) (1 - P^i_{\rm esc})^{n^i_q} (P^i_{\rm esc})^{d\mathrm{n}^i + d\mathrm{z}^i - n^i_q} \sigma^i_{\rm abr}(\mathrm{Z}_{\mathrm{PF}^i}, \mathrm{A}_{\mathrm{PF}^i}). \tag{3.1}$$

The calculation of the excitation energy, $E^*_{\mathrm{PF}^i}$, corresponding to each cross section, $\sigma^i_{\rm abr}(\mathrm{Z}_{\mathrm{PF}^i}, \mathrm{A}_{\mathrm{PF}^i}, n^i_q)$, in the distribution is described in Section 3.2.3.

Struck Nucleon Escape Probability

When a nucleon is struck during abrasion, it can either scatter into the nucleus or immediately escape the volume of interest. The average probability of escape, P^i_{esc}, is recommended to be 0.5 by Townsend et al. [41]. This value seems to work well for most reactions, as it assumes no curvature on the nuclear surface. In the case of a single nucleon escape, $P^i_{\text{esc}} = 0.72$.

3.2.3 Excitation Energy

The pre-fragment excitation energy, $E^*_{\text{PF}^i}$, in [MeV] is calculated as $E^*_{\text{PF}^i} = E^i_{\text{LD}} + E^i_{\text{FSI}}$. Here, E^i_{LD} is the mass difference between the projectile and pre-fragment nucleus using the liquid drop semi-empirical mass formula, and E^i_{FSI} is called the frictional spectator interaction energy [6, 51]. The latter term describes energy deposited into the pre-fragment by particles that were struck during the abrasion process.

Oliveira et al. [37] propose that E^i_{LD} be calculated using only the excess surface energy term from the liquid drop model. Currently, the following approximation is used for the frictional spectator interaction energy, where n_q is the number of struck nucleons scattered into a pre-fragment with mass A_{PF^i}, charge Z_{PF^i}, and neutron number N_{PF^i}.

$$E^i_{\text{FSI}} = \begin{cases} 6.0 n^i_q (\text{A}_{\text{PF}^i})^{1/3}, & (Z_{\text{PF}^i} \leq 26) \\ 10.2 n^i_q (\text{A}_{\text{PF}^i})^{1/3}, & (Z_{\text{PF}^i} > 26) \end{cases} \tag{3.2}$$

3.3 Evaporation Model

The evaporation model built for RAADFRG is a descendant of the legacy FORTRAN evaporation cascade code, EVA [9, 32]. A modernized version of the code has been written, and various aspects of the formalism within have been updated accordingly. A list of pre-fragments, PF^i, generated by the abrasion code, along with their associated cross sections, σ^i_{abr} and excitation energies, $E^*_{\text{PF}^i}$, are passed into the evaporation model. Monte-Carlo (MC) techniques are used to simulate pre-fragment deexcitation via a cascade of light ion

emissions using the Weisskopf-Ewing formalism [50]. To simplify notation, the i is dropped for the remainder of Section 3.3, with the remark that the evaporation-cascade contributions of each pre-fragment/excitation energy configuration are weighted by their associated cross sections and eventually combined. The six allowable emitted particles, denoted by the index j, are consistent with the nomenclature 'light ion' used throughout the rest of the manuscript. Given sufficient excitation energy, the pre-fragment, or 'parent' nucleus, will emit a light ion, leaving behind a residual 'daughter' nucleus. The emitted particle is subsequently scored in a tally using standard MC methods. If the daughter has enough excitation energy, it then becomes the new parent, and the evaporation cascade continues. Once the excitation energy, and/or residual mass, is depleted the remaining residual nucleus is scored, and the cascade is restarted. The excitation energy is considered depleted when there is no longer enough excitation energy to meet the minimum emission kinetic energy for any of the six light ions.

According to [50] the probability, $P_j(\epsilon)$, of emitting a particle, j, with kinetic energy between ϵ and $d\epsilon$ from PF is given by the following.

$$P_j(\epsilon)d\epsilon = \frac{\mathrm{m}_j(2\mathrm{s}_j+1)}{\pi^2\hbar^3}\sigma^c_{j,\mathrm{D}}(\epsilon)\frac{\rho_{\mathrm{D}}(E^*_{\mathrm{D}})}{\rho_{\mathrm{PF}}(E^*_{\mathrm{PF}})}\epsilon d\epsilon \tag{3.3}$$

$$j \in [1,..,6] = [{}^1_0n, {}^1_1p, {}^2\mathrm{H}, {}^3\mathrm{H}, {}^3\mathrm{He}, {}^4\mathrm{He}]$$

Above, E^*_{D}, is the excitation energy of the residual daughter nucleus, D. The nuclear level densities of the daughter and pre-fragment nuclei are represented by ρ_{D} and ρ_{PF}, respectively. The symbol $\sigma^c_{j,\mathrm{D}}(\epsilon)$ denotes the inverse reaction cross section. In this case, it represents the cross section for the daughter nucleus to capture the emitted particle (see Section 3.3.3). The mass and spin of the emitted particle are given as m_j and s_j. Integrating Eq. 3.3 over the interval of allowable kinetic energies, $\epsilon_{\min}$ to $\epsilon_{\max}$, for the emitted particle gives the emission width, Γ_j. The integration limits are defined in Section 3.3.4 once the form of the integrand is explicitly known.

$$\Gamma_j = \int_{\epsilon_{\min}}^{\epsilon_{\max}} P_j(\epsilon)d\epsilon \tag{3.4}$$

It then follows that the total probability of emitting particle j is given as G_j.

$$G_j = \frac{\Gamma_j}{\sum_j \Gamma_j} \tag{3.5}$$

3.3.1 Level Density

The level density, ρ_{A}, of a nucleus of mass A, with excitation energy E^*_{A} used here is a form of the Back-Shifted Fermi Gas Model originally described in Ref. [49], and more specifcally, from the model presented in Ref. [9]. The level density parameter is represented by $\tilde{a}_{\mathrm{A}}$, where $\mathcal{L}$ is an adjustable constant currently set to a value of 20. The coefficient $\mathrm{C(A, E^*_A)}$ is dependent on both the mass and excitation energy of the nucleus in question.

$$\rho_{\mathrm{A}}(E^*_{\mathrm{A}}) = \mathrm{C(A, E^*_A)} e^{2\sqrt{\tilde{a}_{\mathrm{A}}(E^*_{\mathrm{A}})}} \tag{3.6}$$
$$\tilde{a}_{\mathrm{A}} = \frac{\mathrm{A}}{\mathcal{L}}$$

Various forms of $\mathrm{C(A, E^*_A)}$ exist in the literature (see Section 2.1). However, when implemented into the integrand of the emission width, the resulting integral has no closed-form solution. Moreover, it has been theorized that the odd-even behavior observed in fragmentation cross sections is better modeled by subtracting a pairing energy correction, δ_{eff}, from the excitation energy within the exponent of the level density function [9], [17]. This allows us to remove the energy dependence from the coefficient, giving $\mathrm{C(A, E^*_A)} \approx \mathrm{C(A)}$. Since the maximum mass difference between the excited pre-fragment and residual daughter nucleus is four nucleons, generally a small number compared to the mass of the system, we assume that the value of the coefficient does not vary significantly between the two, $\mathrm{C(D)/C(PF)} \approx 1$. However, this assumption is invalid for $\mathrm{A} \lesssim 10$, so the mass dependence is left in the coefficient giving the following expression.

$$\rho_{\mathrm{A}}(E^*_{\mathrm{A}}) = (\tilde{a}_{\mathrm{A}})^{1/4} e^{2\sqrt{\tilde{a}_{\mathrm{A}}(E^*_{\mathrm{A}} - \delta_{\mathrm{eff}})}} \tag{3.7}$$

3.3.2 Pairing Energy Correction

The excitation energy in the exponential term is shifted by a pairing correction corresponding to a characteristic displacement of the ground-state energy due to pairing of nucleons [9, 17]. This characteristic displacement is not necessarily equal to the pairing energy of the residual nucleus. In this model, the characteristic ground-state energy displacement, $\delta^{\text{eff}} = \delta_{\text{D}} + \delta_j$, is a function of contributions from both the residual, δ_{D}, and emitted particle, δ_j. The two contributions are calculated using Eq. 3.8. This implementation ensures that odd-odd nuclei have no pairing correction, and also ensures that the relationship pairing from even-even nuclei is roughly twice that of odd-even nuclei. The absolute magnitude of the liquid drop pairing energy is also conserved for even-even nuclei.

$$\delta_{\text{A}} = \begin{cases} \dfrac{12}{\sqrt{\text{A}}}, & (even - even) \\ \dfrac{6}{\sqrt{\text{A}}}, & (odd - even) \\ 0, & (odd - odd) \end{cases} \tag{3.8}$$

3.3.3 Capture Cross Section

The cross section for a capture of particle j by nucleus D is represented by $\sigma^{c}_{j,\text{D}}(\epsilon)$ [9],

$$\sigma^{c}_{j,\text{D}}(\epsilon) = \alpha_j \Big(1 + \frac{\beta_j}{\epsilon}\Big)\sigma^{g}_{j,\text{D}}. \tag{3.9}$$

Where the geometric cross section is given as $\sigma^{g}_{j,\text{D}}$,

$$\sigma^{g}_{j,\text{D}} = \begin{cases} \pi(\text{R}_0\text{A}_{\text{D}}^{1/3})^2, & (j = 1, 2) \\ \pi(\text{R}_0\text{A}_{\text{D}}^{1/3} + \zeta)^2, & (j =\geq 3) \end{cases} \quad \text{where,} \quad \begin{matrix} \zeta = 1.2\text{fm} \\ \text{R}_0 = 1.5\text{fm} \end{matrix}. \tag{3.10}$$

The parameterizations for α_j and β_j are acquired from [9] as follows:

$$\alpha_j = \begin{cases} 0.76 + 2.2{\text{A}_{\text{PF}}}^{-1/3}, & (j = 1) \\ 1 + c_j, & (j =\geq 2) \end{cases} \tag{3.11}$$

and,

$$\beta_j[\mathrm{MeV}] = \begin{cases} \dfrac{2.12\mathrm{A}_{\mathrm{PF}}^{-2/3} - 0.5}{\alpha_j}, & (j = 1) \\ -\mathrm{k}_j\mathrm{V}_j, & (j =\geq 2). \end{cases} \tag{3.12}$$

The Coulomb barrier is given by, $\mathrm{k}_j\mathrm{V}_j$. The charged particle parameters k_j and c_j are interpolated from Table A.1, and V_j is obtained as

$$\mathrm{V}_j = \frac{Z_j Z_{\mathrm{D}}(1.439202[\mathrm{MeV} - \mathrm{fm}])}{\mathrm{R}_0\mathrm{A}_{\mathrm{D}}^{1/3} + \zeta}. \tag{3.13}$$

3.3.4 Emission Width

To obtain the emission width for a particular particle emission channel, Eq. 3.4 must be evaluated using the expressions for Eqns. 3.9 and 3.7,

$$\Gamma_j = \int_{\epsilon_{\min}}^{\epsilon_{\max}} \frac{\mathrm{m}_j(2\mathrm{s}_j + 1)}{\pi^2\hbar^3}\sigma_{j,\mathrm{D}}^{c}(\epsilon)\frac{\rho_{\mathrm{D}}(E_{\mathrm{D}}^*)}{\rho_{\mathrm{PF}}(E_{\mathrm{PF}}^*)}\epsilon d\epsilon. \tag{3.14}$$

Above, E_{D}^* is the excitation energy of the daughter nucleus post emission, and E_{PF}^* is the excitation energy of the parent nucleus before the emission. Upon further substitution, Eq. 3.14 becomes

$$\Gamma_j = \frac{\mathrm{m}_j(2\mathrm{s}_j + 1)}{\pi^2\hbar^3}\alpha_j\sigma_{j,\mathrm{D}}^{g}\int_{\epsilon_{\min}}^{\epsilon_{\max}}(\epsilon + \beta_j)\frac{\mathrm{C(D)}}{\mathrm{C(PF)}}\frac{e^{2\sqrt{\tilde{a}_{\mathrm{A}}(E_{\mathrm{A}}^* - \delta_{\mathrm{eff}})}}}{e^{2\sqrt{\tilde{a}_{\mathrm{PF}}(E_{\mathrm{PF}}^*)}}}d\epsilon. \tag{3.15}$$

The pairing correction for the pre-fragment nucleus is ignored, as it has already implemented either in a prior emission or in the excitation energy from abrasion. Rearranging Eq. 3.15 gives,

$$\Gamma_j = \alpha_j\sigma_{j,\mathrm{D}}^{g}e^{-2\sqrt{\tilde{a}_{\mathrm{PF}}(E_{\mathrm{PF}}^*)}}\left(\frac{\tilde{a}_{\mathrm{A_{PF}}}}{\tilde{a}_{\mathrm{A_D}}}\right)^{1/4}\frac{\mathrm{m}_j(2\mathrm{s}_j + 1)}{\pi^2\hbar^3}\int_{\epsilon_{\min}}^{\epsilon_{\max}}(\epsilon + \beta_j)e^{2\sqrt{\tilde{a}_{\mathrm{A}}(E_{\mathrm{A}}^* - \delta_{\mathrm{eff}})}}d\epsilon. \tag{3.16}$$

Using the relationship that $E_{\mathrm{D}}^* = E_{\mathrm{PF}}^* - Q_j - \epsilon$, where Q_j is the Q-value for the reaction, 3.16 may be expressed as the following integral:

$$\Gamma_j = \alpha_j\sigma_{j,\mathrm{D}}^{g}e^{-2\sqrt{\tilde{a}_{\mathrm{PF}}(E_{\mathrm{PF}}^*)}}\left(\frac{\tilde{a}_{\mathrm{A_{PF}}}}{\tilde{a}_{\mathrm{A_D}}}\right)^{1/4}\frac{\mathrm{m}_j(2\mathrm{s}_j + 1)}{\pi^2\hbar^3}\int_{\epsilon_{\min}}^{E_{\mathrm{PF}}^* - Q_j - \epsilon - \delta_{\mathrm{eff}}}(\epsilon + \beta_j)e^{2\sqrt{\tilde{a}_{\mathrm{A}}(E_{\mathrm{A}}^* - \delta_{\mathrm{eff}})}}d\epsilon. \tag{3.17}$$

For charged particles $\epsilon_{\min} = \mathrm{k}_j \mathrm{V}_j$, and for neutrons $\epsilon_{\min} = 0$. Performing the integration gives Eqns. 3.18 and 3.19 the following expressions for the neutron and charged particle emission widths. Below, $\mathcal{R}_j$ represents the maximum allowable kinetic energy of the emitted particle, and n implies $j = 1$. Below, $\mathcal{R}_n = E^*_{\mathrm{PF}} - Q_n - \delta_{\mathrm{eff}}$, and $\mathcal{R}_j = E^*_{\mathrm{PF}} - Q_j - \mathrm{k}_j \mathrm{V}_j - \delta_{\mathrm{eff}}$.

$$\Gamma_n = \frac{\mathrm{m}_n(2\mathrm{s}_n+1)}{\hbar^3}(\mathrm{R}_0\mathrm{A}_\mathrm{D}^{1/3})^2\alpha_n\Big(\frac{\tilde{a}_{\mathrm{A_{PF}}}}{\tilde{a}_{\mathrm{A_D}}}\Big)^{1/4}\frac{e^{-2\sqrt{\tilde{a}_{\mathrm{PF}}(E^*_{\mathrm{PF}})}}}{(4\tilde{a}_{\mathrm{A_D}})^2}\Bigg[-2e^2\sqrt{\tilde{a}_{\mathrm{A_D}}\mathcal{R}_n} \Bigg(-4\tilde{a}_{\mathrm{A_D}}\Big(2\sqrt{\tilde{a}_{\mathrm{A_D}}\mathcal{R}_n}-1\Big)\Big(\beta_n+\mathcal{R}_n\Big)+(4\tilde{a}_{\mathrm{A_D}}\mathcal{R}_n)^{3/2}-12\tilde{a}_{\mathrm{A_D}}\mathcal{R}_n+ 12\sqrt{\tilde{a}_{\mathrm{A_D}}\mathcal{R}_n}-6\Bigg)+8\tilde{a}_{\mathrm{A_D}}(\beta_n+\mathcal{R}_n)-12\Bigg] \tag{3.18}$$

$$\Gamma_j = \frac{\mathrm{m}_j(2\mathrm{s}_j+1)}{\hbar^3}(\mathrm{R}_0\mathrm{A}_\mathrm{D}^{1/3}+\zeta)^2\alpha_n\Big(\frac{\tilde{a}_{\mathrm{A_{PF}}}}{\tilde{a}_{\mathrm{A_D}}}\Big)^{1/4}\frac{e^{-2\sqrt{\tilde{a}_{\mathrm{PF}}(E^*_{\mathrm{PF}})}}}{(4\tilde{a}_{\mathrm{A_D}})^2}\Bigg[-2e^2\sqrt{\tilde{a}_{\mathrm{A_D}}\mathcal{R}_j} \Bigg(-4\tilde{a}_{\mathrm{A_D}}\Big(2\sqrt{\tilde{a}_{\mathrm{A_D}}\mathcal{R}_j}-1\Big)\Big(\mathcal{R}_n\Big)+(4\tilde{a}_{\mathrm{A_D}}\mathcal{R}_n)^{3/2}-12\tilde{a}_{\mathrm{A_D}}\mathcal{R}_n+ 12\sqrt{\tilde{a}_{\mathrm{A_D}}\mathcal{R}_j}-6\Bigg)+8\tilde{a}_{\mathrm{A_D}}\mathcal{R}_j-12\Bigg] \tag{3.19}$$

3.3.5 Emission Kinetic Energy and Angle

Once the emitted particle identity is selected, we determine its kinetic energy, ϵ, and emission angle, Ω. The kinetic energy is sampled from a probability density function calculated from Eq. 3.3. The emission energy and angle are sampled from the reference frame of the residual nucleus. Therefore, these values must be converted back to the rest frame of the projectile nucleus center of mass using conservation of momentum, before being scored as double differential cross section contributions. However, since this work is primarily concerned with total yield, a description of the transformation is not included.

3.4 Coalescence Model

At relativistic energies, the inelastic reaction cross section consists of the abrasion cross section and the electromagnetic dissociation cross section. During the abrasion process (Section 3.2), nucleons in the overlap region are removed from the projectile nucleus, leaving behind an excited pre-fragment. Within the scope of coalescence, only the abraded nucleons are of concern. The excited pre-fragment is handed off to the evaporation-cascade model (Section 3.3). The coalescence model developed for this nuclear fragmentation code is a modified form of one implemented in Ref. [1], as it is also derived from the formalism initially proposed by Awes et al. [3]. Abraded nucleons that occupy the coalescence volume, in momentum space, are assumed to coalesce and form a light ion. Those outside the coalescence volume remain unchanged. The previous model included both abrasion and ablation nucleons together in forming light ions through by means of the coalescence mechanism. In this formalism, coalescence cross section contributions for light ions are calculated for each abrasion reaction channel individually, and are subsequently summed over all abrasion channels to get total contributions. As illustrated further on, this prevents the non-physical coalescence of particles not created simultaneously from the same parent within the same abrasion reaction channel. It also allows for a more accurate prescription of the relationship between nucleon multiplicity distributions available to coalescence within each abrasion channel.

3.4.1 Abraded Nucleon Cross Sections

The total abrasion cross section, $\sigma_{\mathrm{abr}}^{\mathrm{tot}}$ is calculated as the summation over all individual abrasion reaction channels, i, given by

$$\sigma_{\mathrm{abr}}^{\mathrm{tot}} = \sum_{i} \sigma_{\mathrm{abr}}^{i}. \tag{3.20}$$

Above, $\sigma_{\mathrm{abr}}^{i}$ is the cross section for the abrasion reaction in which $d\mathrm{n}^{i}$ neutrons and $d\mathrm{z}^{i}$ protons are removed from the projectile nucleus, producing an excited pre-fragment, PF^{i}, with mass $A_{\mathrm{PF}^{i}}$. Using A_{parent} to represent either the projectile or target nucleus in question,

the pre-fragment mass number is calculated as $A_{\mathrm{PF}^i} = A_{\mathrm{parent}} - (d\mathrm{n}^i + d\mathrm{z}^i)$. The pre-fragment exists as an intermediate state, continuing on to undergo ablation if given sufficient excitation energy. Similarly the abraded proton and neutron multiplicities are represented by $\bar{m}^i_{(1,0)}$ and $\bar{m}^i_{(0,1)}$, and are respectively calculated as

$$\begin{aligned} d\mathrm{n}^i &= N_{\mathrm{parent}} - N_{\mathrm{PF}^i} = \bar{m}^i_{(0,1)} \\ d\mathrm{z}^i &= Z_{\mathrm{parent}} - Z_{\mathrm{PF}^i} = \bar{m}^i_{(1,0)}. \end{aligned} \tag{3.21}$$

The differential multiplicity distribution of any particle k produced in the abrasion reaction channel i is represented by $\frac{d^3\mathcal{N}^i_k}{d\mathrm{p}^3}$. It relates the differential yield cross section distribution, $\frac{d^3\sigma^i_k}{d\mathrm{p}^3}$, to the reaction channel cross section, σ^i_{abr} using

$$\frac{d^3\mathcal{N}^i_k}{d\mathrm{p}^3} = \frac{1}{\sigma^i_{\mathrm{abr}}} \frac{d^3\sigma^i_k}{d\mathrm{p}^3}. \tag{3.22}$$

3.4.2 Coalesced Particle Multiplicity

The differential multiplicity distribution for a coalesced particle with Z protons, N neutrons, and mass number A, is represented by

$$\frac{d^3\mathcal{N}^i(Z,N)}{d\mathrm{p}^3} = \frac{\bar{M}^i_{(Z,N)}}{N!Z!} \left(\frac{4\pi}{3} P^i_0(Z,N)^3\right)^{A-1} \left[\frac{d^3\mathcal{N}^i(0,1)}{d\mathrm{p}^3}\right]^N \left[\frac{d^3\mathcal{N}^i(1,0)}{d\mathrm{p}^3}\right]^Z. \tag{3.23}$$

This prescription has been adapted from its original form as presented in Ref. [1] to be implemented separately for each abrasion channel. In Eq. 3.23, $\frac{d^3\mathcal{N}^i(0,1)}{d\mathrm{p}^3}$ and $\frac{d^3\mathcal{N}^i(1,0)}{d\mathrm{p}^3}$ represent the differential multiplicity distributions for abraded neutrons and protons in reaction channel i, respectively. The average multiplicity of the composite particle is represented by $\bar{M}^i_{(Z,N)}$. The relativistic coefficient is represented by the symbol, γ. This equation is evaluated in the rest frame of the projectile, therefore $\gamma \approxeq 1$. The term $\left(\frac{4\pi}{3} P^i_0(Z,N)^3\right)$ is the coalescence volume. The parameter $P^i_0(Z,N)$ is termed the coalescence radius and signifies the radius, in momentum space [MeV/c], of the coalescence volume. This parameter is of significant importance, as all nucleons occupying the coalescence volume

are considered to coalesce to form a composite nucleus (see Section 3.4.4). Assuming the differential neutron multiplicity distribution has the same spectral shape in momentum space as the differential proton multiplicity distribution, they are related by

$$\frac{d^3\mathcal{N}^i(0,1)}{d\mathrm{p}^3} = \left(\frac{\bar{m}^i_{(0,1)}}{\bar{m}^i_{(1,0)}}\right)\frac{d^3\mathcal{N}^i(1,0)}{d\mathrm{p}^3}. \tag{3.24}$$

3.4.3 Coalescence Cross Sections

In order to determine which nucleons occupy the coalescence volume, the differential nucleon multiplicity distributions must be explicitly known and also be integrable. Experimental observations show that collision fragment distributions exhibit Gaussian behavior in transverse momentum [15]. Therefore, it is reasonable to assume the abraded nucleon distribution is also Gaussian in the rest frame of their parent nucleus. Analogously, the differential cross section for abraded protons is

$$\frac{d^3\sigma^i(1,0)}{d\mathrm{p}^3} = \sigma^i(1,0)\left[\frac{1}{\left(2\pi\triangle^{i2}\right)^{3/2}}\right]e^{\left(-\frac{\mathrm{p}^2}{2\triangle^{i2}}\right)}, \tag{3.25}$$

where $\sigma^i(1,0)$ is the cross section for producing a single proton in the coalescence volume. These distributions have been studied in some detail and parameteric forms have been developed to describe describe final fragment momentum shifts and widths [20, 21, 22, 43, 46]. The parameterization of fragment distribution variance, represented by $\triangle^{i2}$ [MeV/c], used in this model is a form of the Goldhaber Model [12] modified by Tripathi and Townsend [45] to include projectile and target mass as well as beam kinetic energy. The variance is given by

$$\triangle^{i2} = \triangle_0^{i\,2}(d\mathrm{n}^i + d\mathrm{z}^i)(A_{\mathrm{parent}} - (d\mathrm{n}^i + d\mathrm{z}^i))/(A_{\mathrm{parent}} - 1), \tag{3.26}$$

where

$$\triangle_0^{i\,2} = (1 + E_C/4T_{\mathrm{lab}})(70 + 2A_{\mathrm{parent}}/3), \tag{3.27}$$

and

$$E_C = \frac{Z_{\text{parent}} Z_{\text{other}} 1.439202[\text{MeV} - \text{fm}]}{\text{R}_0(A_{\text{parent}}^{1/3} + A_{\text{other}}^{1/3})}. \tag{3.28}$$

Above, E_C is the average Coulomb energy of the colliding system, A_{other} is the counterpart nucleus participating in the collision with A_{parent}, and T_{lab} is the beam energy of the projectile in MeV/A.

Combining (3.23) and (3.25), followed by applying the condition from Eq. (3.24) to both the proton and composite particle differential multiplicity distributions yields a relationship of their respective differential cross sections. Furthermore, since this formalism is interested only in total yield cross sections, the composite particle cross section differential momentum distribution must be integrated over momentum. However, before this can be done, the relation $d\text{p}^3_{(Z,N)} = (A \cdot d\text{p})^3$ must be applied. Inserting this relation to the previously described combined equation yields

$$\frac{d^3\sigma^i_{\text{coal}}(Z,N)}{d\text{p}^3} = \frac{\bar{M}^i_{(Z,N)}}{N!Z!}\left(\frac{4\pi}{3\sigma^i_{\text{abr}}} P_0^i(Z,N)^3\right)^{A-1}\left(\frac{\bar{m}^i_{(0,1)}}{\bar{m}^i_{(1,0)}}\right)^N\left[\frac{\sigma^i(1,0)}{\left(2\pi\triangle^{i^2}\right)^{3/2}}\right]^A A^3 e^{\left(-\frac{A\text{p}^2}{2\triangle^{i^2}}\right)}. \tag{3.29}$$

Integrating over momentum gives an expression for the coalescence cross section for abrasion channel i,

$$\sigma^i_{\text{coal}}(Z,N) = \frac{\bar{M}^i_{(Z,N)}}{N!Z!}\left(\frac{4\pi}{3\sigma^i_{\text{abr}}} P_0^i(Z,N)^3\right)^{A-1}\left(\frac{\bar{m}^i_{(0,1)}}{\bar{m}^i_{(1,0)}}\right)^N \frac{A^{3/2}}{\left(2\pi\triangle^{i^2}\right)^{\frac{3}{2}(A-1)}}\sigma^i(1,0)^A. \tag{3.30}$$

In this form, the composite particle coalescence cross section, $\sigma^i_{\text{coal}}(Z,N)$, is expressed in terms of known values, apart from its average multiplicity, $\bar{M}^i_{(Z,N)}$. Since this composite particle multiplicity term is not explicitly known, the equation must be manipulated in order to be of use. To do so, we use the technique implemented by [1]. Dividing $\sigma^i_{\text{coal}}(Z,N)$

by both $\bar{M}^i_{(Z,N)}$ and the cross section for producing a single proton in the coalescence region, $\sigma^i(1,0)$, yields the composite particle production fraction per abraded nucleon,

$$F^i(Z,N) = \frac{1}{N!Z!}\Big(\frac{4\pi}{3\sigma^i_{\rm abr}}P^i_0(Z,N)^3\Big)^{A-1}\Big(\frac{\bar{m}^i_{(0,1)}}{\bar{m}^i_{(1,0)}}\Big)^N \frac{A^{3/2}\sigma^i(1,0)^{A-1}}{(2\pi\triangle^{i2})^{\frac{3}{2}(A-1)}}. \tag{3.31}$$

The production fraction shown in Eq. 3.31 is then multiplied by the coalescence-corrected multiplicity weighted proton cross section, $\sigma^i_{\rm coal}(1,0)$, to get the coalescence cross section, $\sigma^i_{\rm coal}(Z,N)$, with multiplicity implicitly included to get

$$\sigma^i_{\rm coal}(Z,N) = \frac{1}{N!Z!}\Big(\frac{4\pi}{3\sigma^i_{\rm abr}}P^i_0(Z,N)^3\Big)^{A-1}\Big(\frac{\bar{m}^i_{(0,1)}}{\bar{m}^i_{(1,0)}}\Big)^N \frac{A^{3/2}\sigma^i(1,0)^{A-1}}{(2\pi\triangle^{i2})^{\frac{3}{2}(A-1)}}\sigma^i_{\rm coal}(1,0). \tag{3.32}$$

However, Eq. 3.32 requires still further manipulation to be of implementable form since the value of $\sigma^i_{\rm coal}(1,0)$ is not yet explicitly known. One advantage of performing this calculation over a set of discrete abrasion reaction channels is that this equation may be simplified in the following manner. In all abrasion channels satisfying the condition $\bar{m}^i_{(1,0)} \neq 0$, the condition $\sigma^i(1,0) = \sigma^i_{\rm abr}$ also holds. Applying this relation and dividing both sides by $\sigma^i_{\rm coal}(1,0)$ yields the ratio of final coalesced particle cross section to the final proton cross section from abrasion,

$$\frac{\sigma^i_{\rm coal}(Z,N)}{\sigma^i_{\rm coal}(1,0)} = \frac{1}{N!Z!}\Big(\frac{4\pi}{3}P^i_0(Z,N)^3\Big)^{A-1}\Big(\frac{\bar{m}^i_{(0,1)}}{\bar{m}^i_{(1,0)}}\Big)^N \frac{A^{3/2}}{(2\pi\triangle^{i2})^{\frac{3}{2}(A-1)}}. \tag{3.33}$$

Logic has been incorporated in order to prevent the coalescence of unphysical composite particles. For example, the code does not allow for ^{3}He or ^{4}He production via the coalescence mechanism if less than two protons were abraded. More plainly stated, $\sigma^i_{\rm coal}(Z,2) \equiv 0$ when $\bar{m}^i_{(0,1)} < 2$. Similarly, $\sigma^i_{\rm coal}(2,N) \equiv 0$ when $\bar{m}^i_{(1,0)} < 2$.

Furthermore, nucleon conservation along each reaction channel is ensured by using

$$\begin{aligned}\sigma(1,0)^i_{\text{coal}} &= \bar{m}^i_{(1,0)}\sigma^i_{\text{abr}} - \Big[\sigma^i_{\text{coal}}(1,1) + \sigma^i_{\text{coal}}(1,2) + 2[\sigma^i_{\text{coal}}(2,1) + \sigma^i_{\text{coal}}(2,2)]\Big] \\ \sigma(0,1)^i_{\text{coal}} &= \bar{m}^i_{(0,1)}\sigma^i_{\text{abr}} - \Big[\sigma^i_{\text{coal}}(1,1) + \sigma^i_{\text{coal}}(2,1) + 2[\sigma^i_{\text{coal}}(1,2) + \sigma^i_{\text{coal}}(2,2)]\Big].\end{aligned} \tag{3.34}$$

Equation 3.34 may be expressed in matrix form as

$$\begin{bmatrix} 1 & \left[\frac{\sigma^i_{\text{coal}}(1,1)}{\sigma^i_{\text{coal}}(1,0)} + 2\frac{\sigma^i_{\text{coal}}(1,2)}{\sigma^i_{\text{coal}}(1,0)} + \frac{\sigma^i_{\text{coal}}(2,1)}{\sigma^i_{\text{coal}}(1,0)} + 2\frac{\sigma^i_{\text{coal}}(2,1)}{\sigma^i_{\text{coal}}(1,0)}\right] \\ 0 & \left[1 + \frac{\sigma^i_{\text{coal}}(1,1)}{\sigma^i_{\text{coal}}(1,0)} + \frac{\sigma^i_{\text{coal}}(1,2)}{\sigma^i_{\text{coal}}(1,0)} + 2\frac{\sigma^i_{\text{coal}}(2,1)}{\sigma^i_{\text{coal}}(1,0)} + 2\frac{\sigma^i_{\text{coal}}(2,1)}{\sigma^i_{\text{coal}}(1,0)}\right] \end{bmatrix} \begin{bmatrix} \sigma^i_{\text{coal}}(0,1) \\ \sigma^i_{\text{coal}}(1,0) \end{bmatrix} = \begin{bmatrix} \bar{m}^i_{(0,1)} \\ \bar{m}^i_{(1,0)} \end{bmatrix} \sigma^i_{\text{abr}}. \tag{3.35}$$

Eq. 3.33 conveniently makes it possible to solve for $\sigma^i_{\text{coal}}(0,1)$ and $\sigma^i_{\text{coal}}(1,0)$ in Eq. 3.35. At this point, $\sigma(Z,N)^i_{\text{coal}}$ may then be evaluated as the product of Eq. 3.33 and $\sigma^i_{\text{coal}}(1,0)$ for each coalesced species. The total yield cross section for a coalesced light ion, $\sigma^{\text{tot}}_{\text{coal}}(Z,N)$, is calculated by summing over the contributions of all abrasion reaction channels,

$$\sigma^{\text{tot}}_{\text{coal}}(Z,N) = \sum_i \frac{\sigma^i_{\text{coal}}(Z,N)}{\sigma^i_{\text{coal}}(1,0)}. \tag{3.36}$$

3.4.4 Coalescence Radius

During the instant immediately preceding the conclusion of an abrasion event, all participating nucleons are considered to behave as unbound particles. Abraded nucleons occupying the same coalescence volume in momentum space are assumed to coalesce into a composite nucleus, forming a light ion. The coalescence radius, $P^i_0(Z,N)$, is a parameter commonly used to represent the radius of a sphrical volume in momentum space. A number of values for coalescence radii have been proposed and measured throughout literature [28, 4, 25, 39, 3, 2, 27, 33]. Generally, these models use parameterizations based on reaction participants and their energies. Most of these formalisms, including those in which coalescence values are extracted from experimental data [4, 3] consider the coalescence to occur as one averaged event over all impact parameters. This makes them incompatible with

the formalism derived in this work. Because of the model-dependent parametric nature, values that yield reasonable agreement with experimental data with one model will likely not perform as well when implemented using another formalism. For this reason, a new parametric form of $P_0^i(Z,N)$ has been developed and is described in this section.

In the formalism introduced in Sections 3.4.1-3.4.3, coalescence is assumed to occur on a point in both space and time. As such, no inherent consideration for the spacial distance between abraded nucleons has been made as of yet. Thus, an accounting for spatial effects has been wrapped into the parameterization of $P_0^i(Z,N)$ magnitude. No physical justification is claimed for this parameterization beyond sufficient reproduction of experimentally measured cross section data. In this model, the shape of the vector $\vec{P_0^i}$ is fixed, and the magnitude of each component is uniformly scaled using a power function of A_{parent} and A_{other}. The coalescence radius is calculated as

$$\begin{aligned} \vec{P_0^i} &= \langle P_0^i(1,1), P_0^i(1,2), P_0^i(2,1), P_0^i(2,2)\rangle \\ &= \langle 238.95, 310.5, 346.95, 453.6\rangle A_{\text{other}}^{-0.206} A_{\text{parent}}^{-0.172} \end{aligned} \tag{3.37}$$

3.5 Electromagnetic Dissociation

This phenomenon occurs when there is no spatial overlap between the collision participants and the projectile nucleus passes within close enough proximity to interact significantly via the Coulomb force. Nucleons and light ions will dissociate from the projectile nucleus if the magnitude of the Coulomb interaction is strong enough to overcome their specific binding energy within the projectile. Norbury and Adamczyk [35] have derived a formalism for calculating double-differential electromagnetic dissociation cross sections in nucleus-nucleus collisions. This section is not discussed in great detail in this dissertation. The code and formalism for this mechanism are the work of John W. Norbury from NASA Langley Research Center.

Chapter 4

Results and Conclusion

4.1 Evaporation Results

An example of the total evaporation yields is given in Figure 4.1 below. The energy reported here is the particle's kinetic energy in the rest frame of the pre-fragment nucleus. These results include both evaporated and final residual nucleus contributions. The Coulomb barrier effects are seen clearly for the lighter charged particles. The subsequent three illustrations show how these total yields are distributed in angle and energy. The angular results presented here are not corrected for solid angle, giving rise to a peak at 90 degrees. If a solid angle normalization is included, the magnitude of the double differential cross sections are uniform in emission angle per energy bin. Since this work is concerned only with total yields, a more thorough analysis of the double differential production cross section results is deferred to future investigation.

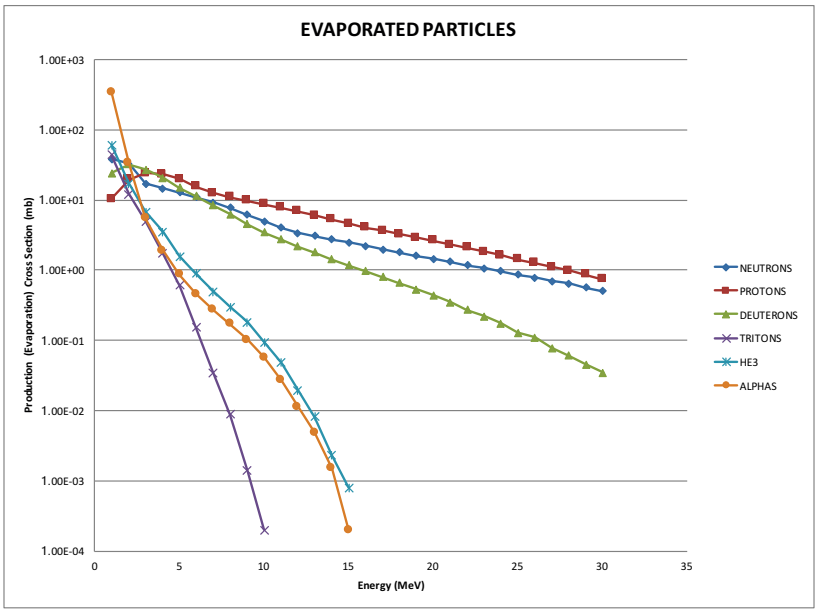


Figure 4.1: Light ion production from evaporation in the reaction of ^{12}C on ^{12}C at a beam energy of 1572 MeV/A.

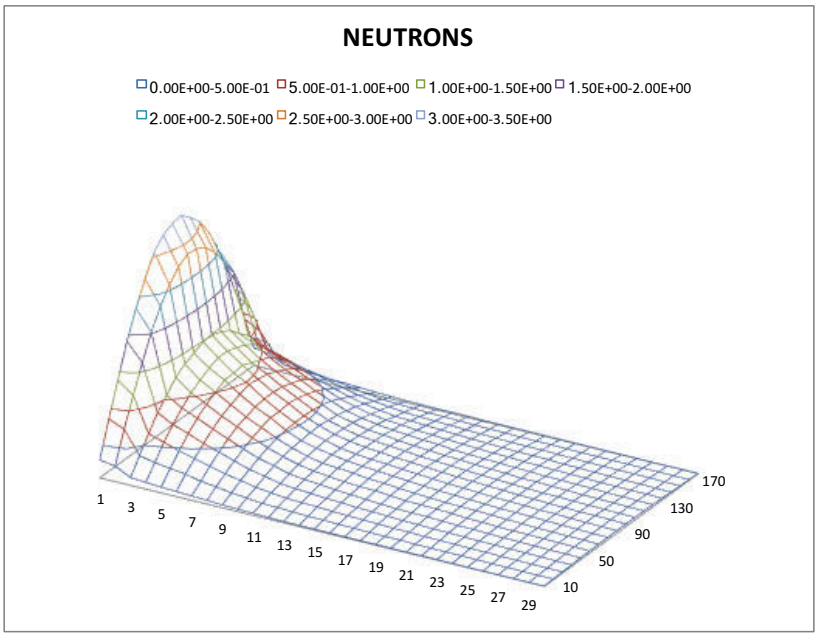


Figure 4.2: Neutron production from evaporation in the reaction of ^{12}C on ^{12}C at a beam energy of 1572 MeV/A. The vertical axis is cross section (mb), the right axis is emitted angle (degrees), and the left axis is emitted energy (MeV).

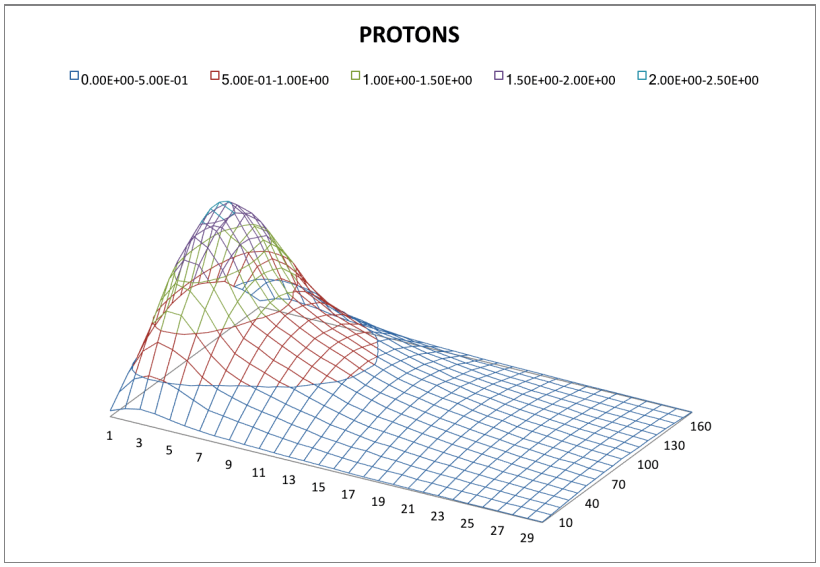


Figure 4.3: Proton production from evaporation in the reaction of ^{12}C on ^{12}C at a beam energy of 1572 MeV/A. The vertical axis is cross section (mb), the right axis is emitted angle (degrees), and the left axis is emitted energy (MeV).

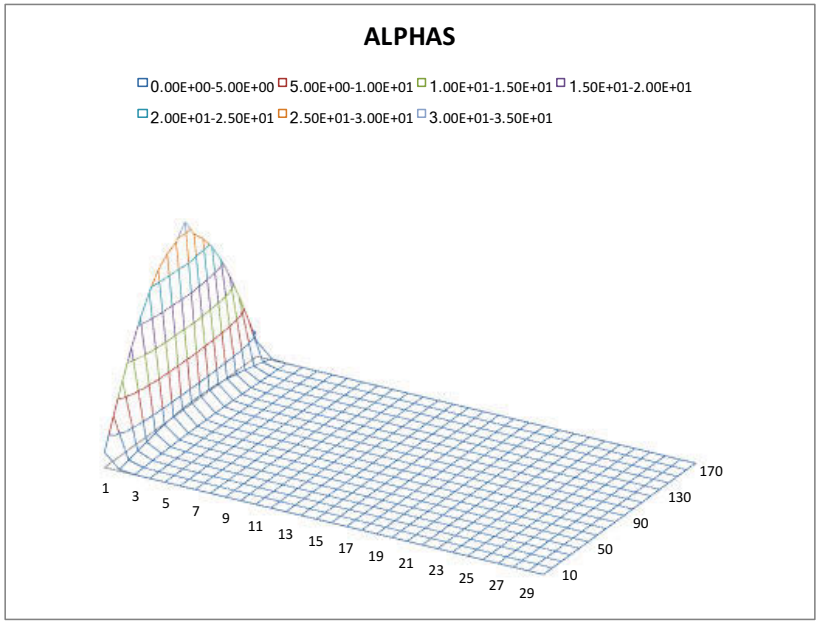


Figure 4.4: Alpha production from evaporation in the reaction of ^{12}C on ^{12}C at a beam energy of 1572 MeV/A. The vertical axis is cross section (mb), the right axis is emitted angle (degrees), and the left axis is emitted energy (MeV).

4.2 Coalescence Results

Presented in this section is a comparison of RAADFRG total light ion yield and experimentally measured values. Correct reproduction of experimental light ion data requires that all three light ion production mechanisms function properly. Since the energies and projectiles shown in this section are not expected to have significant electromagnetic dissociation cross sections, these results serve as a record of coalescence model performance. The projectiles shown in this section include ^{12}C and ^{16}O with incident beam energies between 290 MeV/A and 2100 MeV/A. The target nuclei consist of ^{9}Be, ^{12}C, ^{27}Al, ^{64}Cu, and ^{207}Pb. Note, the H-1 experimental cross section measurements reported in Figures 4.8 and 4.11 were performed within a shallow angle of the incident beam and therefore do not represent total yield cross sections. Furthermore, while neutron production cross section measurements for these reactions were not reported, the RAADFRG predicted neutron production cross sections are still provided.

No comparisons with experimental data are made for neutrons in this study. However, the calculated neutron yields are included in the figures in this section because a comparison with the calculated proton yields is useful. In each of the figures below, the proton and neutron yields are roughly equivalent. Since both projectile species are symmetric in proton and neutron abundance, this result is expected. According to these results, the coalescence model implemented in RAADFRG is able to consistently reproduce the experimental results over a wide range of beam energies and target masses. The parameterization of coalescence radius describes the spatial effects for both symmetric and largely asymmetric collision systems for intermediate and high energies. In is not clear however, how well this parameterization will hold for systems with beam energies less than 100 MeV/A.

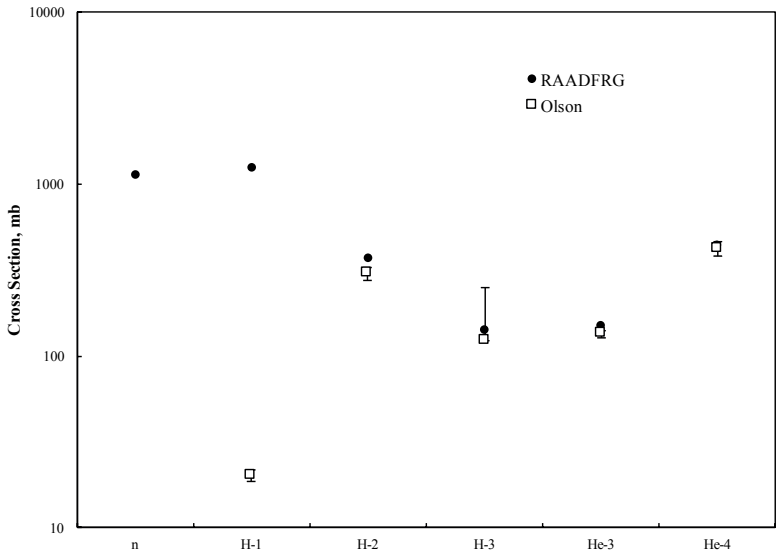


Figure 4.5: A comparison of light ion production cross sections from RAADFRG and experimental measurements from Ref. [38] for the collision reaction: ^{12}C on ^{9}Be at 290 MeV/A.

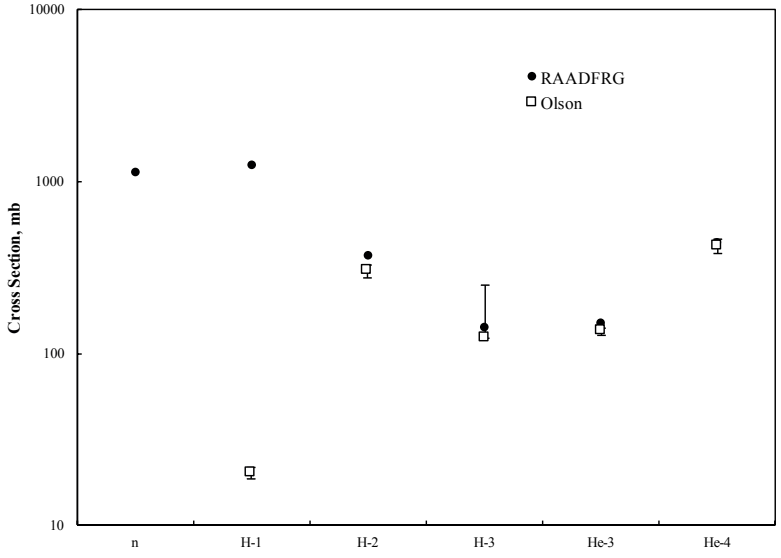


Figure 4.6: A comparison of light ion production cross sections from RAADFRG and experimental measurements from Ref. [38] for the collision reaction: ^{12}C on ^{9}Be at 1050 MeV/A.

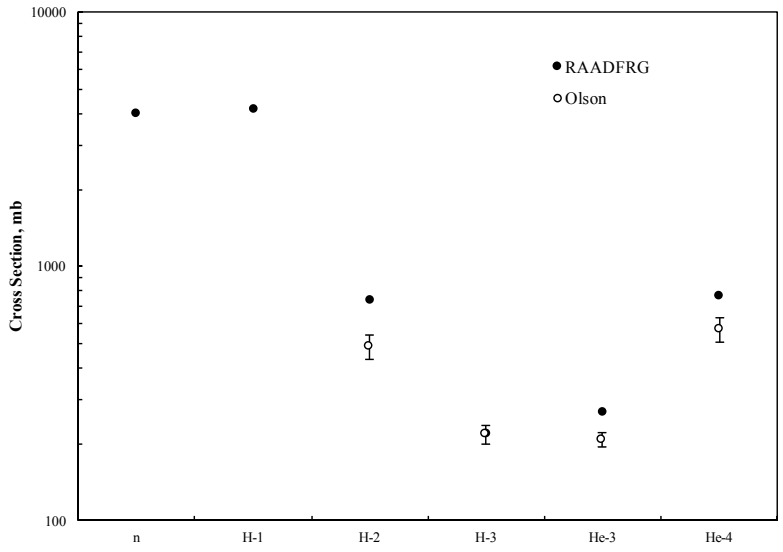


Figure 4.7: A comparison of light ion production cross sections from RAADFRG and experimental measurements from Ref. [38] for the collision reaction: ^{12}C on ^{64}Cu at 1050 MeV/A.

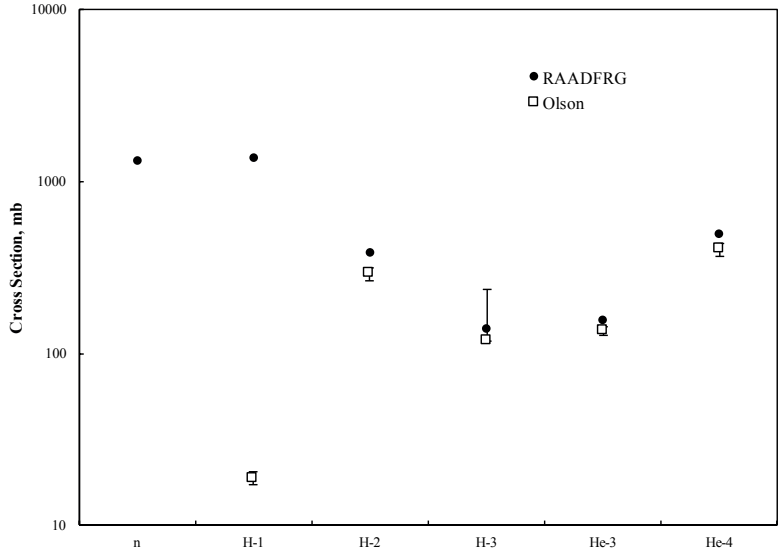


Figure 4.8: A comparison of light ion production cross sections from RAADFRG and experimental measurements from Ref. [38] for the collision reaction: ^{12}C on ^{12}C at 1050 MeV/A.

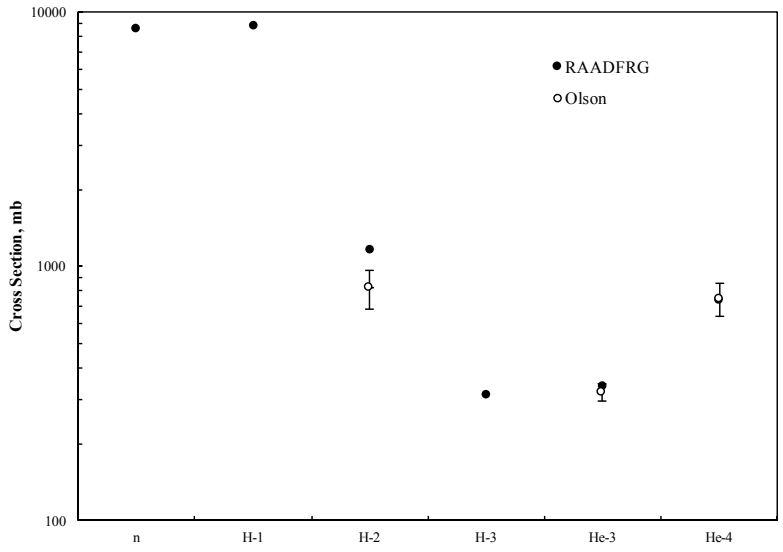


Figure 4.9: A comparison of light ion production cross sections from RAADFRG and experimental measurements from Ref. [38] for the collision reaction: ^{12}C on ^{207}Pb at 1050 MeV/A.

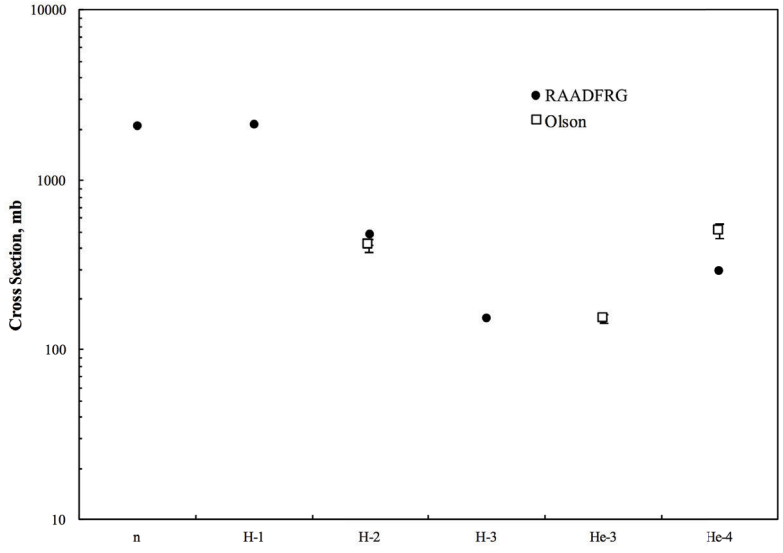


Figure 4.10: A comparison of light ion production cross sections from RAADFRG and experimental measurements from Ref. [38] for the collision reaction: ^{16}O on ^{9}Be at 2100 MeV/A.

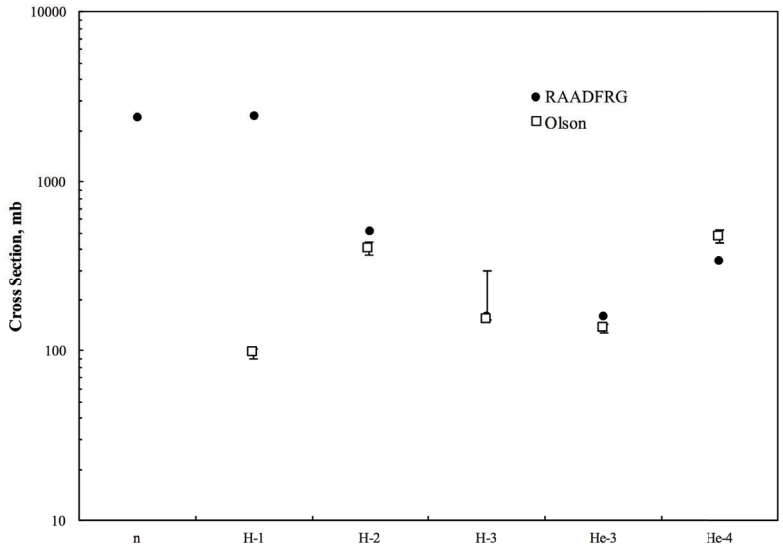


Figure 4.11: A comparison of light ion production cross sections from RAADFRG and experimental measurements from Ref. [38] for the collision reaction: ^{16}O on ^{12}C at 2100 MeV/A.

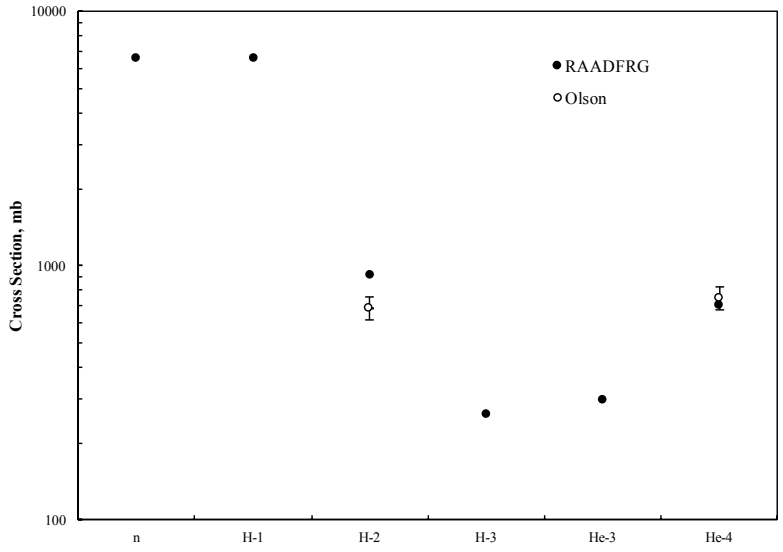


Figure 4.12: A comparison of light ion production cross sections from RAADFRG and experimental measurements from Ref. [38] for the collision reaction: ^{16}O on ^{64}Cu at 2100 MeV/A.

4.3 Elemental and Isotopic Production Cross Sections

Comparisons of elemental production cross sections with various experimentally measured values are reported in this section. Figures 4.13-4.52 display elemental production cross sections for fragment species with a charge of Be or greater. Similarly, Figures 4.53-4.59 display isotopic production cross sections for projectiles of ^{12}C, ^{16}O, ^{36}Ar, and ^{40}Ar at various beam energies incident on either ^{9}Be and ^{12}C targets. Lines are drawn between data points in the figures for this section to aid in identifying trends in the data. However, no interpolation is implied.

With the pairing energy correction discussed in Section 3.3.2, RAADFRG consistently reproduces the even-odd behavior exhibited in experimental results. However, the calculated results systematically over-predict production of elements with a charge within one or two protons of the beam charge. This is likely due to inconsistencies between theory and reality for the assumed excitation energy of the initial pre-fragment when removing single nucleons. This notion is supported by an apparent over-depletion of the on-beam charge production cross section bin.

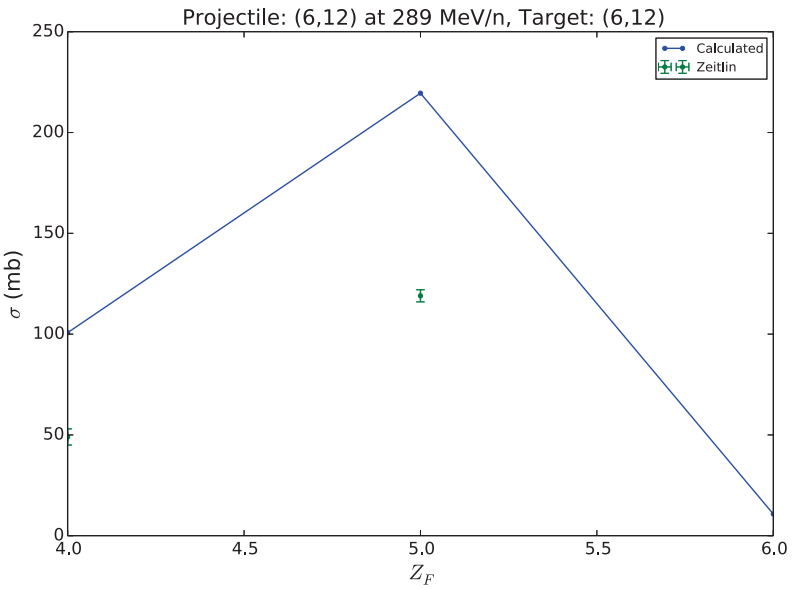


Figure 4.13: Elemental production cross sections (solid) compared with experimental measurements (error bars) from Ref. [53] for the reaction of ^{12}C on ^{12}C at 289 MeV/A.

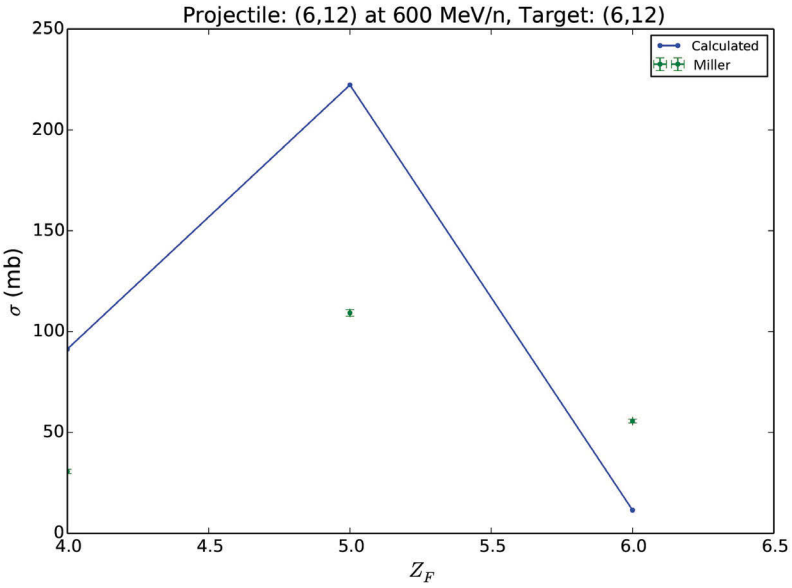


Figure 4.14: Elemental production cross sections (solid) compared with experimental measurements (error bars) from Ref. [29] for the reaction of ^{12}C on ^{12}C at 600 MeV/A.

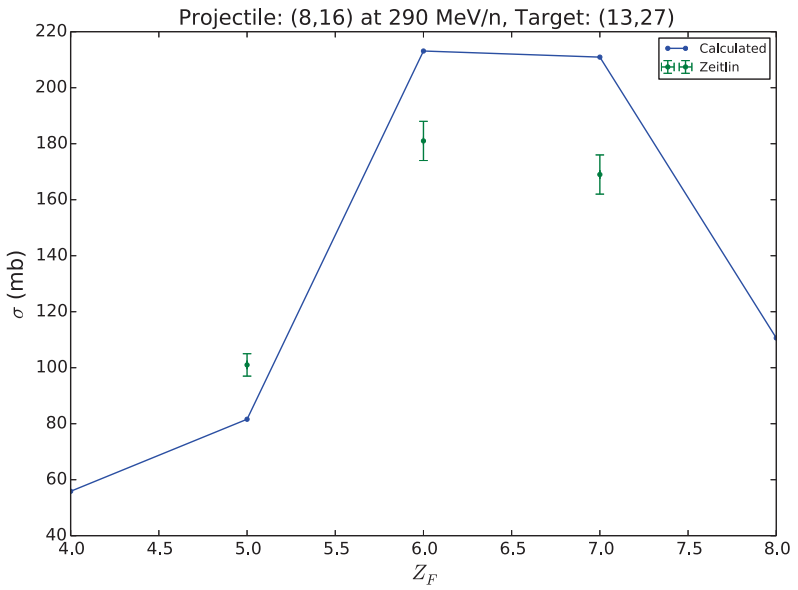


Figure 4.15: Elemental production cross sections (solid) compared with experimental measurements (error bars) from Ref. [55] for the reaction of ^{16}O on ^{27}Al at 290 MeV/A.

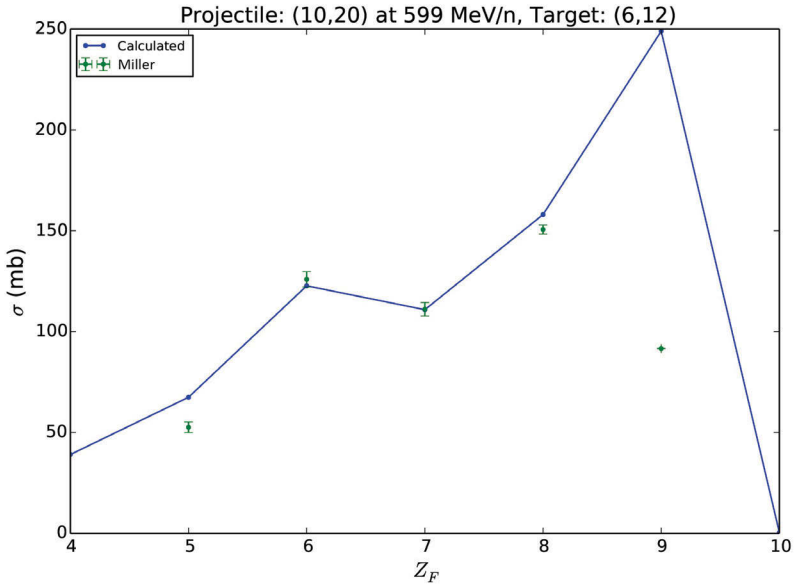


Figure 4.16: Elemental production cross sections (solid) compared with experimental measurements (error bars) from Ref. [29] for the reaction of ^{20}Ne on ^{12}C at 599 MeV/A.

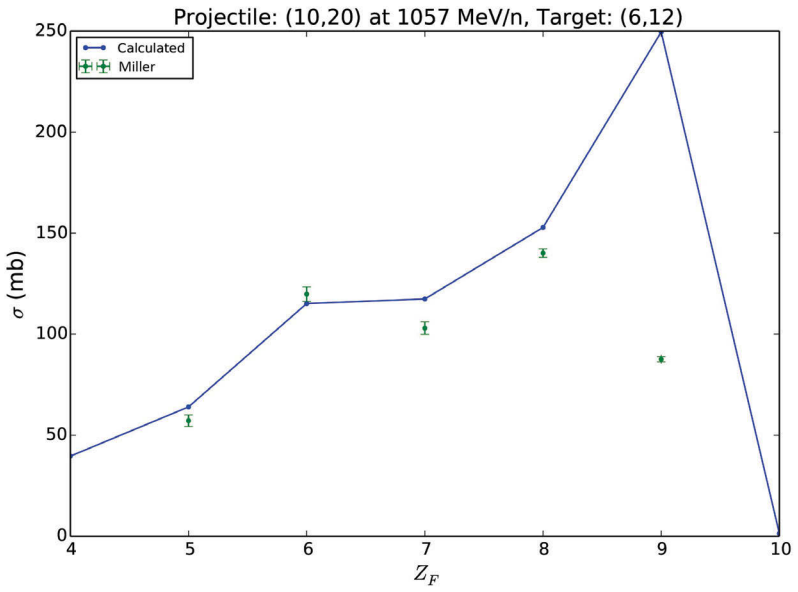


Figure 4.17: Elemental production cross sections (solid) compared with experimental measurements (error bars) from Ref. [29] for the reaction of ^{20}Ne on ^{12}C at 1057 MeV/A.

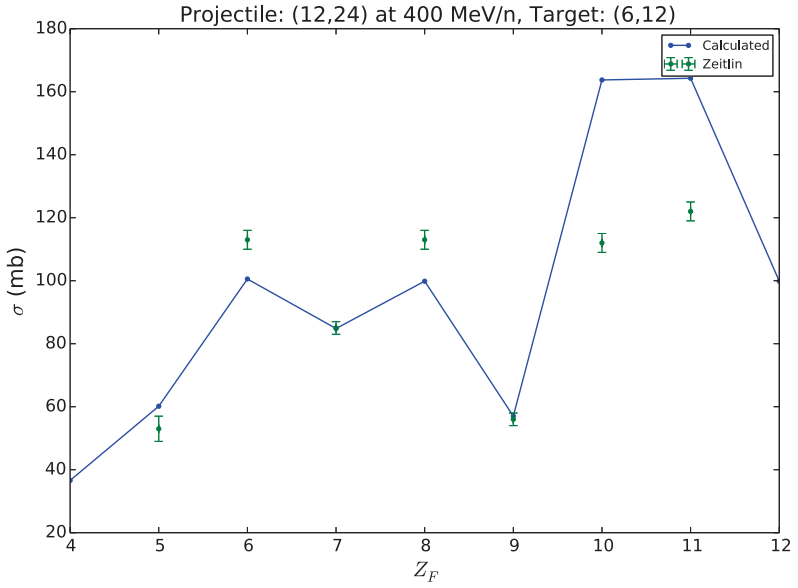


Figure 4.18: Elemental production cross sections (solid) compared with experimental measurements (error bars) from Ref. [55] for the reaction of ^{24}Mg on ^{12}C at 400 MeV/A.

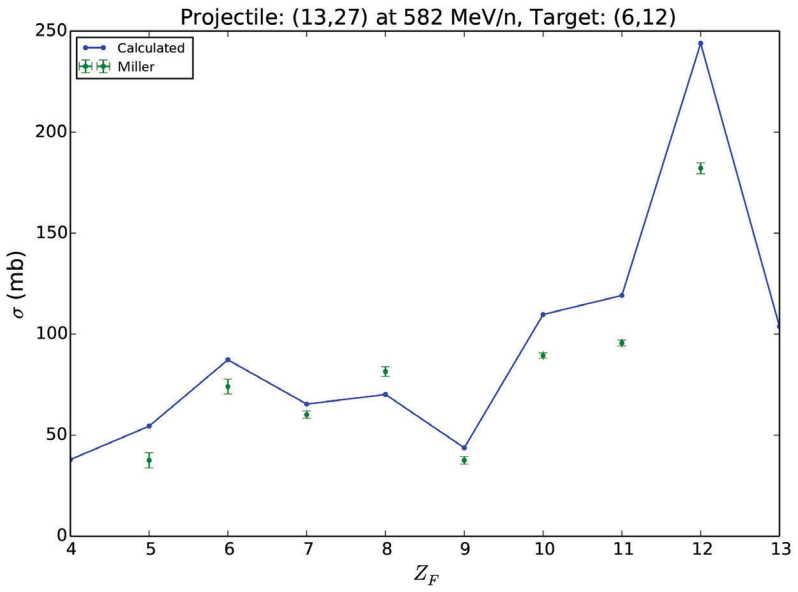


Figure 4.19: Elemental production cross sections (solid) compared with experimental measurements (error bars) from Ref. [29] for the reaction of ^{27}Al on ^{12}C at 582 MeV/A.

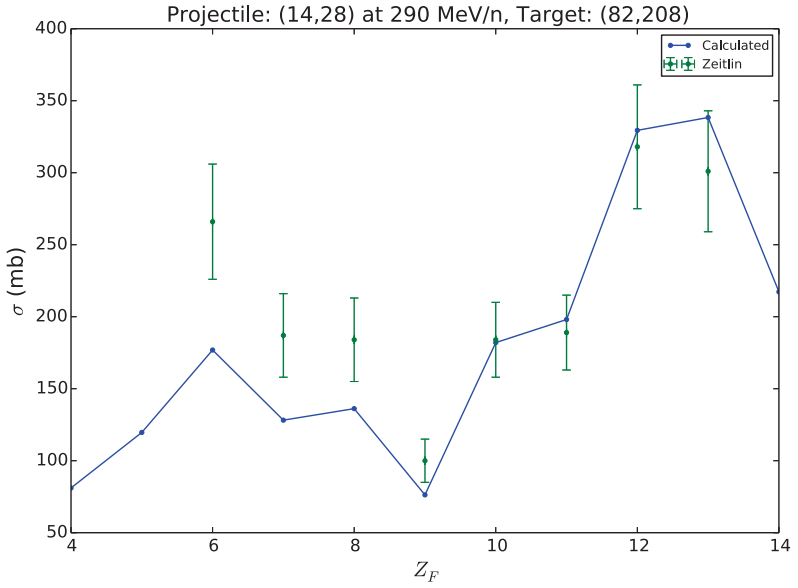


Figure 4.20: Elemental production cross sections (solid) compared with experimental measurements (error bars) from Ref. [52] for the reaction of ^{28}Si on ^{208}Pb at 290 MeV/A.

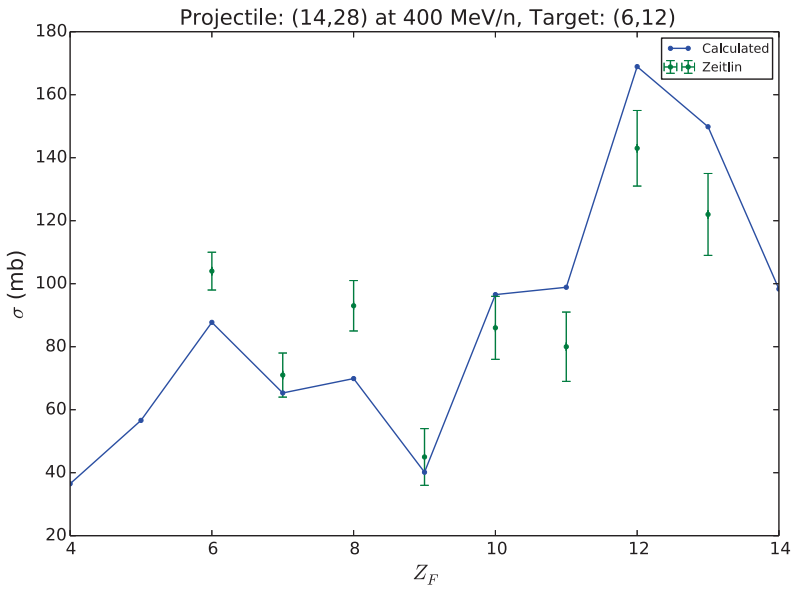


Figure 4.21: Elemental production cross sections (solid) compared with experimental measurements (error bars) from Ref. [52] for the reaction of ^{28}Si on ^{12}C at 400 MeV/A.

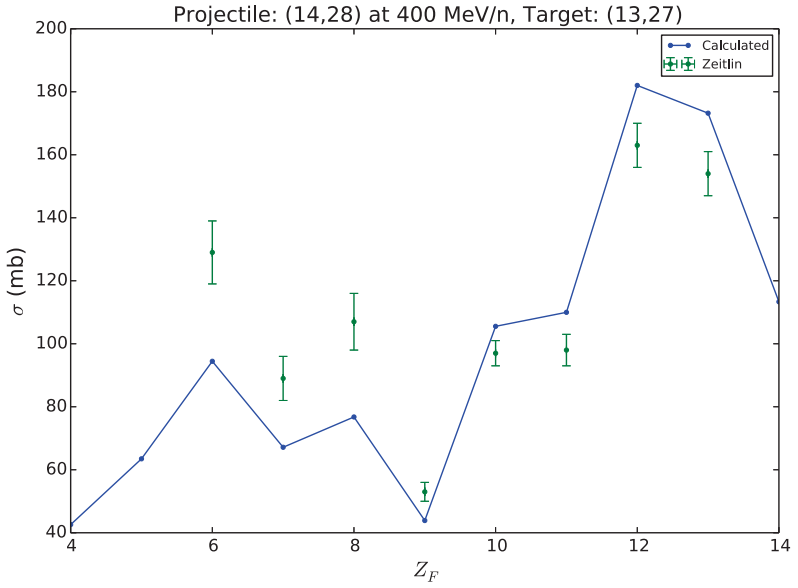


Figure 4.22: Elemental production cross sections (solid) compared with experimental measurements (error bars) from Ref. [52] for the reaction of ^{28}Si on ^{27}Al at 400 MeV/A.

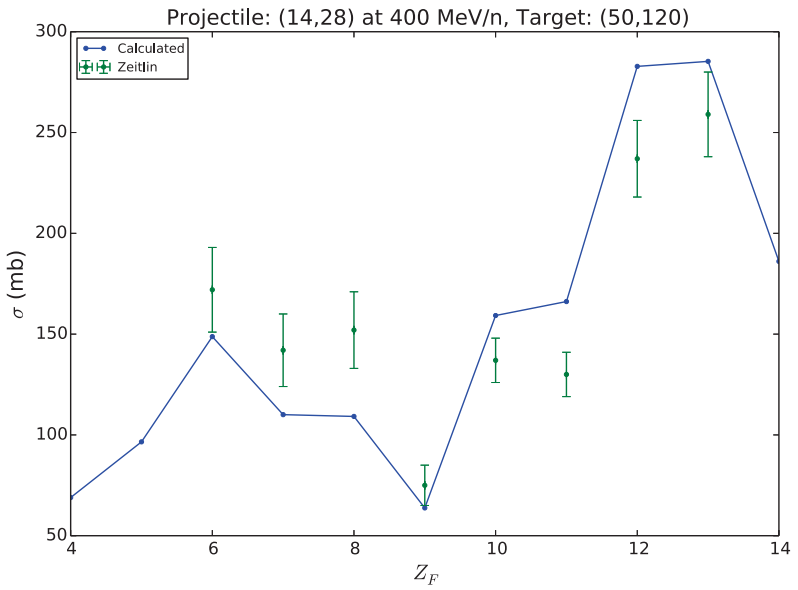


Figure 4.23: Elemental production cross sections (solid) compared with experimental measurements (error bars) from Ref. [52] for the reaction of ^{28}Si on ^{120}Sn at 400 MeV/A.

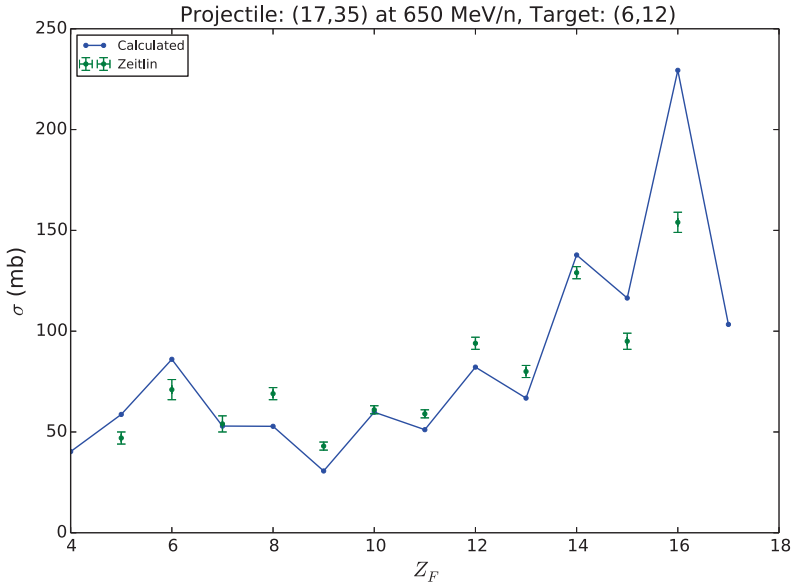


Figure 4.24: Elemental production cross sections (solid) compared with experimental measurements (error bars) from Ref. [54] for the reaction of ^{35}Cl on ^{12}C at 650 MeV/A.

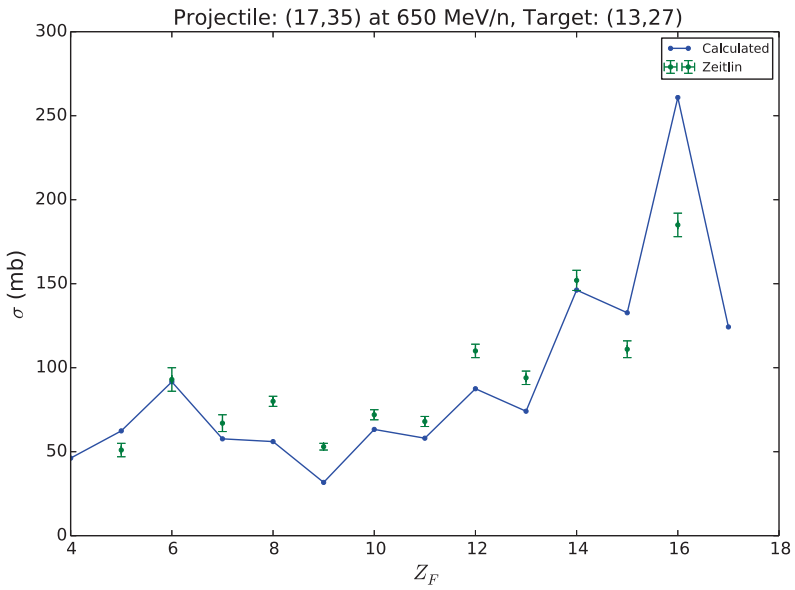


Figure 4.25: Elemental production cross sections (solid) compared with experimental measurements (error bars) from Ref. [54] for the reaction of ^{35}Cl on ^{27}Al at 650 MeV/A.

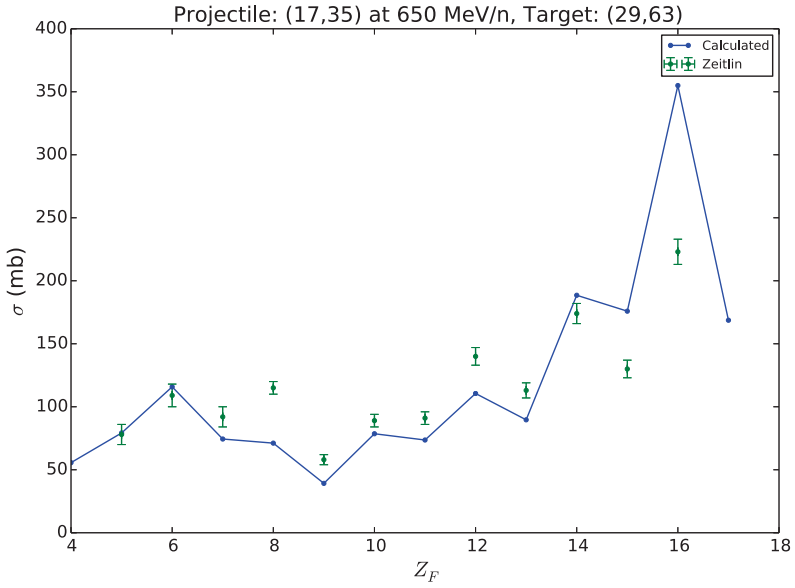


Figure 4.26: Elemental production cross sections (solid) compared with experimental measurements (error bars) from Ref. [54] for the reaction of ^{35}Cl on ^{63}Cu at 650 MeV/A.

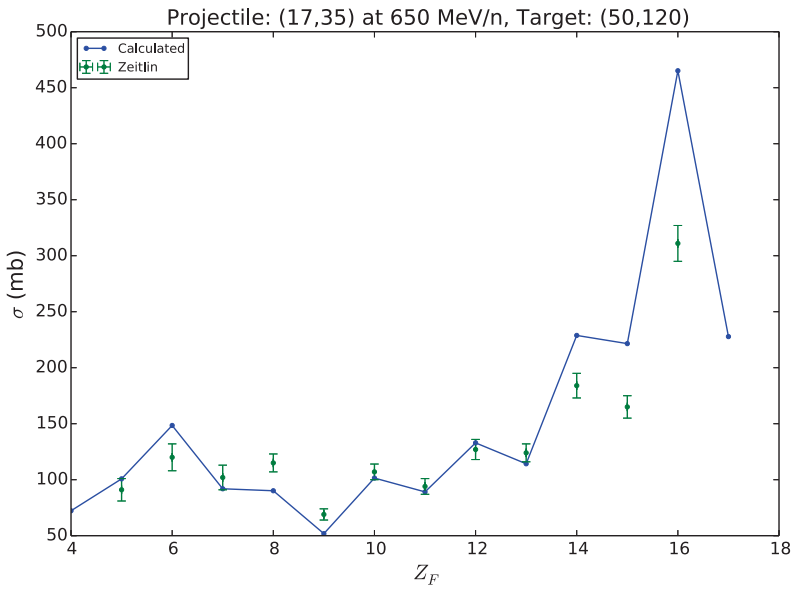


Figure 4.27: Elemental production cross sections (solid) compared with experimental measurements (error bars) from Ref. [54] for the reaction of ^{35}Cl on ^{120}Sn at 650 MeV/A.

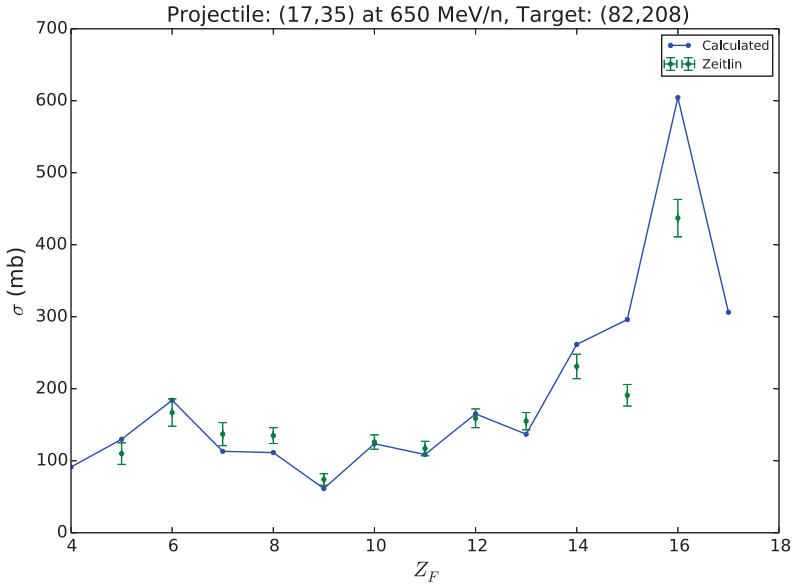


Figure 4.28: Elemental production cross sections (solid) compared with experimental measurements (error bars) from Ref. [54] for the reaction of ^{35}Cl on ^{208}Pb at 650 MeV/A.

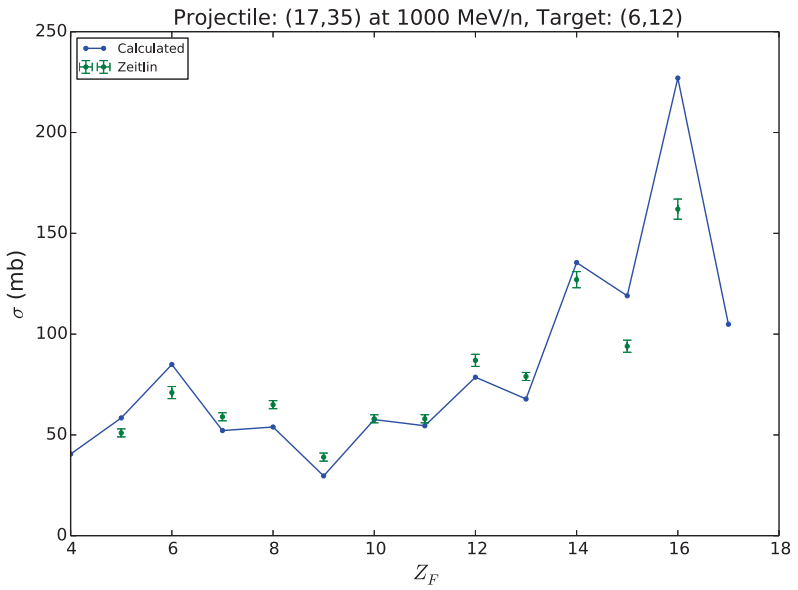


Figure 4.29: Elemental production cross sections (solid) compared with experimental measurements (error bars) from Ref. [54] for the reaction of ^{35}Cl on ^{12}C at 1000 MeV/A.

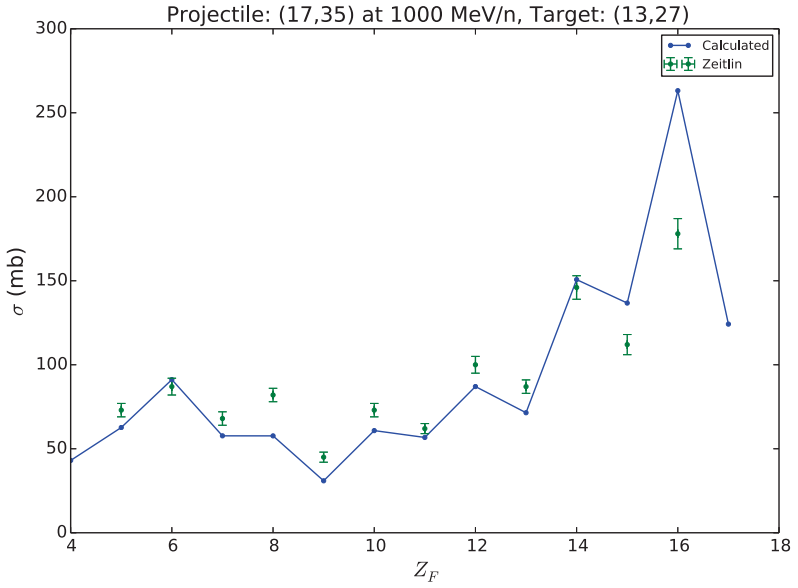


Figure 4.30: Elemental production cross sections (solid) compared with experimental measurements (error bars) from Ref. [54] for the reaction of ^{35}Cl on ^{27}Al at 1000 MeV/A.

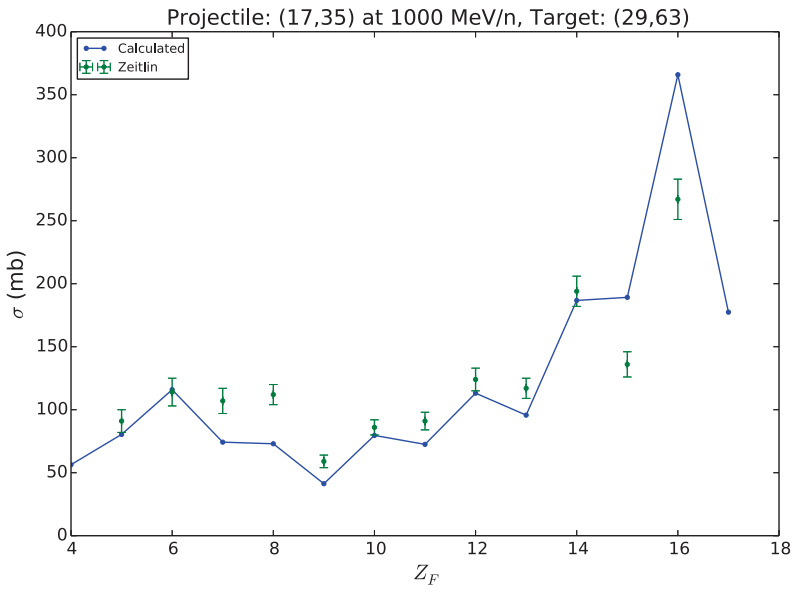


Figure 4.31: Elemental production cross sections (solid) compared with experimental measurements (error bars) from Ref. [54] for the reaction of ^{35}Cl on ^{63}Cu at 1000 MeV/A.

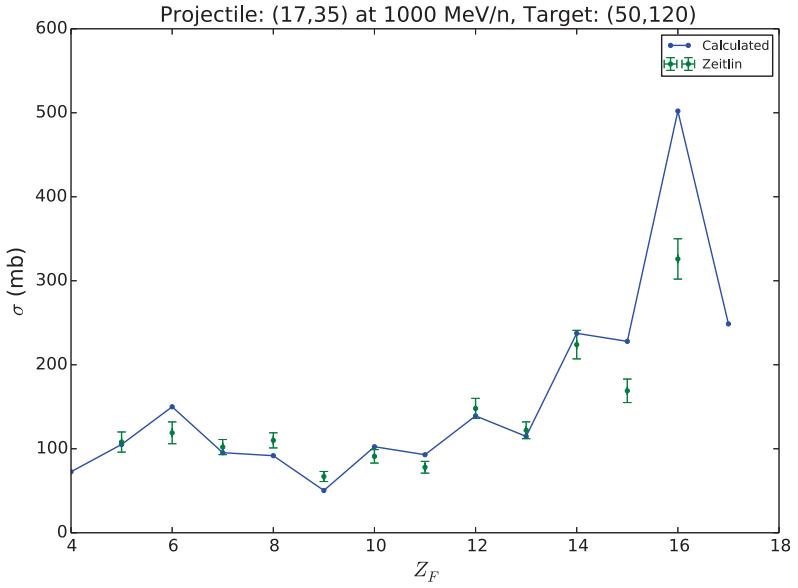


Figure 4.32: Elemental production cross sections (solid) compared with experimental measurements (error bars) from Ref. [54] for the reaction of ^{35}Cl on ^{120}Sn at 1000 MeV/A.

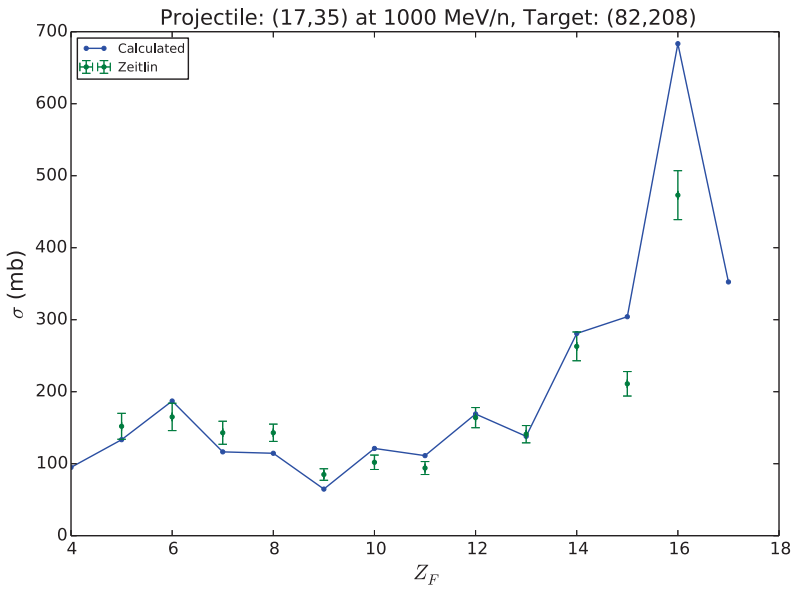


Figure 4.33: Elemental production cross sections (solid) compared with experimental measurements (error bars) from Ref. [54] for the reaction of ^{35}Cl on ^{208}Pb at 1000 MeV/A.

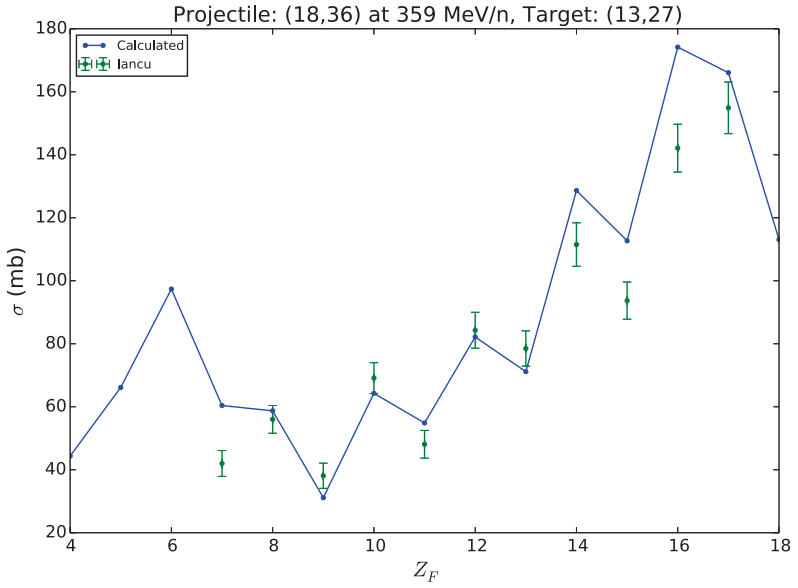


Figure 4.34: Elemental production cross sections (solid) compared with experimental measurements (error bars) from Ref. [18] for the reaction of ^{36}Ar on ^{27}Al at 359 MeV/A.

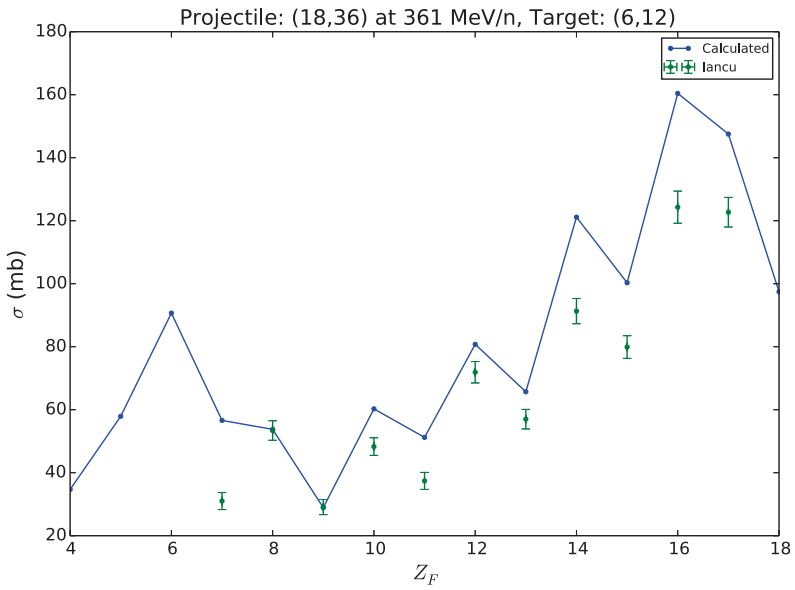


Figure 4.35: Elemental production cross sections (solid) compared with experimental measurements (error bars) from Ref. [18] for the reaction of ^{36}Ar on ^{12}C at 361 MeV/A.

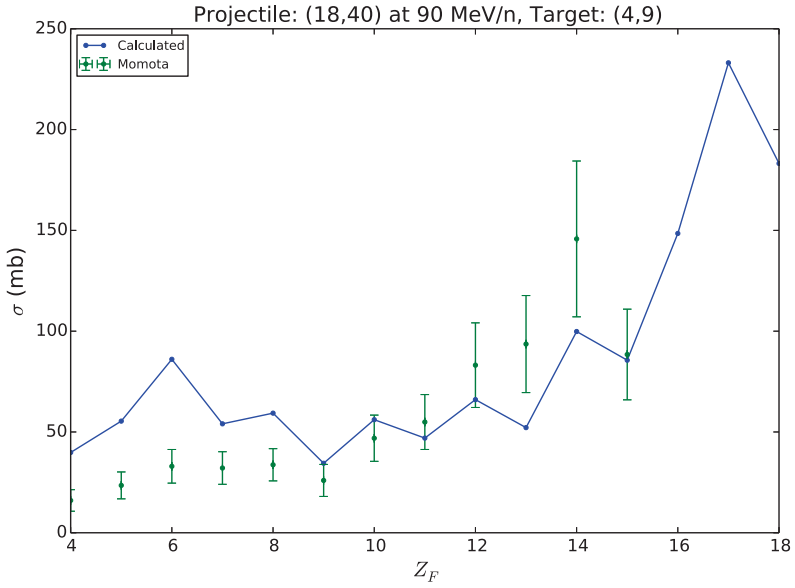


Figure 4.36: Elemental production cross sections (solid) compared with experimental measurements (error bars) from Ref. [31] for the reaction of ^{40}Ar on ^{9}Be at 90 MeV/A.

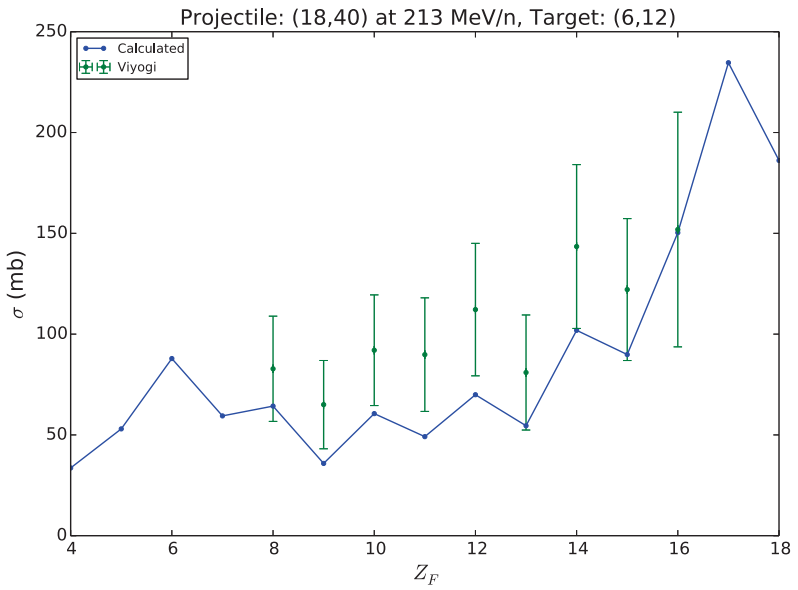


Figure 4.37: Elemental production cross sections (solid) compared with experimental measurements (error bars) from Ref. [47] for the reaction of ^{40}Ar on ^{12}C at 213 MeV/A.

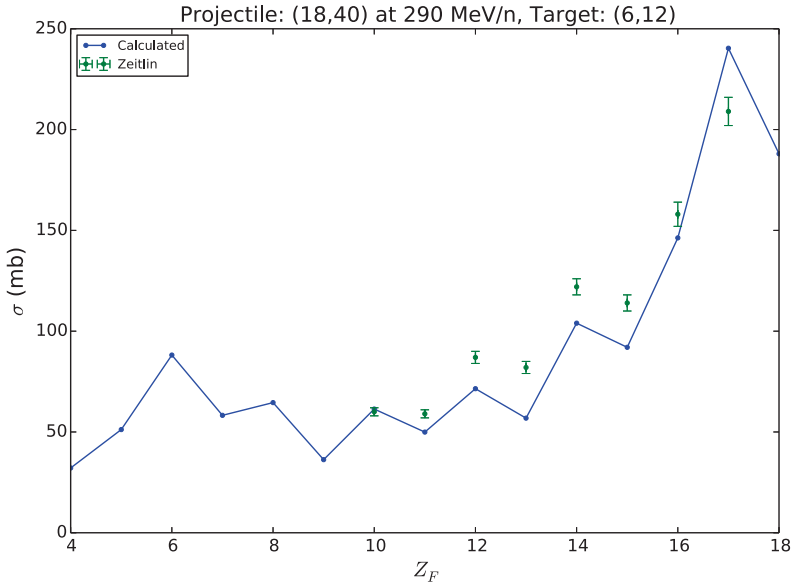


Figure 4.38: Elemental production cross sections (solid) compared with experimental measurements (error bars) from Ref. [54] for the reaction of ^{40}Ar on ^{12}C at 290 MeV/A.

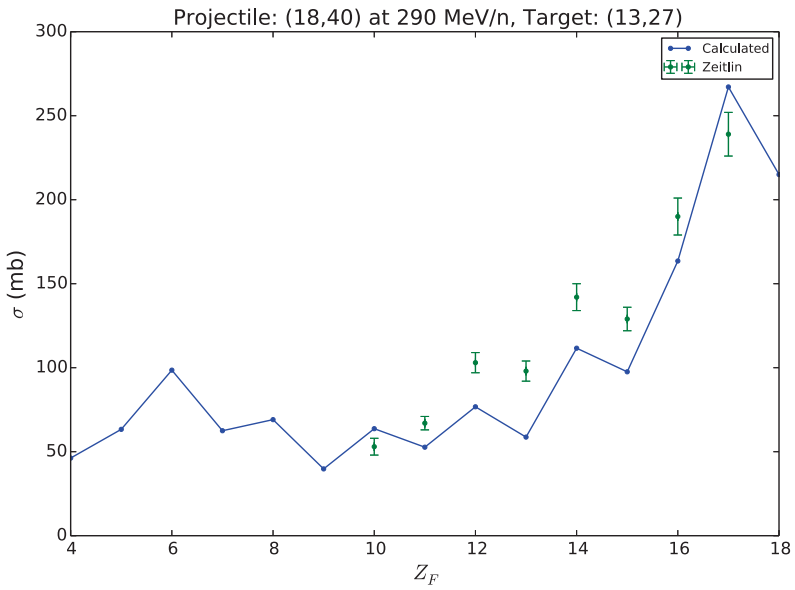


Figure 4.39: Elemental production cross sections (solid) compared with experimental measurements (error bars) from Ref. [54] for the reaction of ^{40}Ar on ^{27}Al at 290 MeV/A.

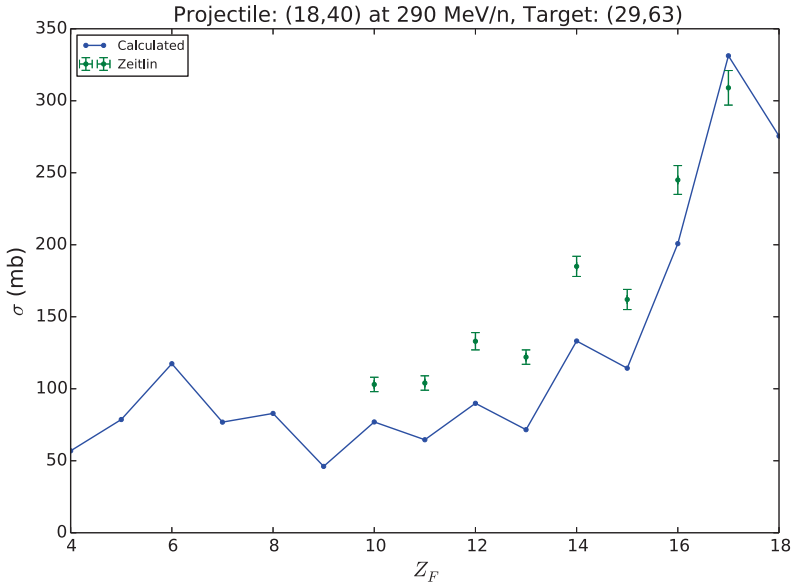


Figure 4.40: Elemental production cross sections (solid) compared with experimental measurements (error bars) from Ref. [54] for the reaction of ^{40}Ar on ^{63}Cu at 290 MeV/A.

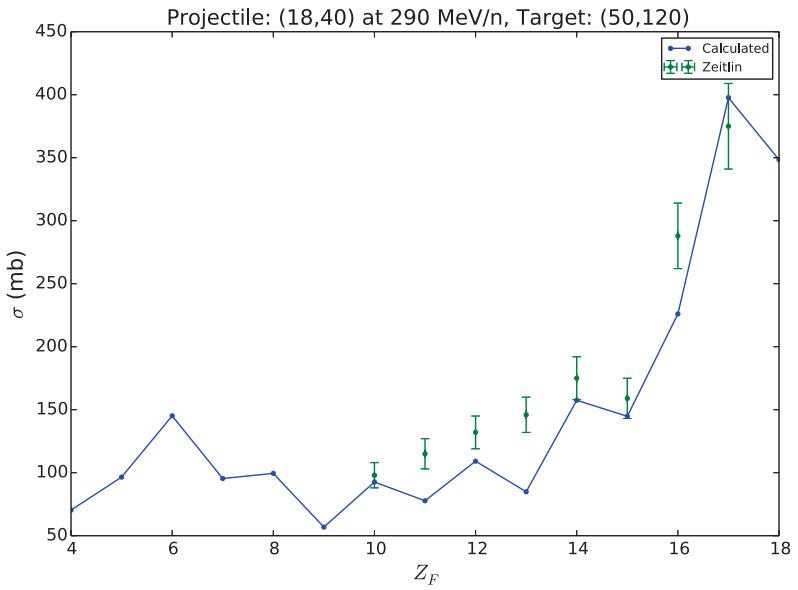


Figure 4.41: Elemental production cross sections (solid) compared with experimental measurements (error bars) from Ref. [54] for the reaction of ^{40}Ar on ^{120}Sn at 290 MeV/A.

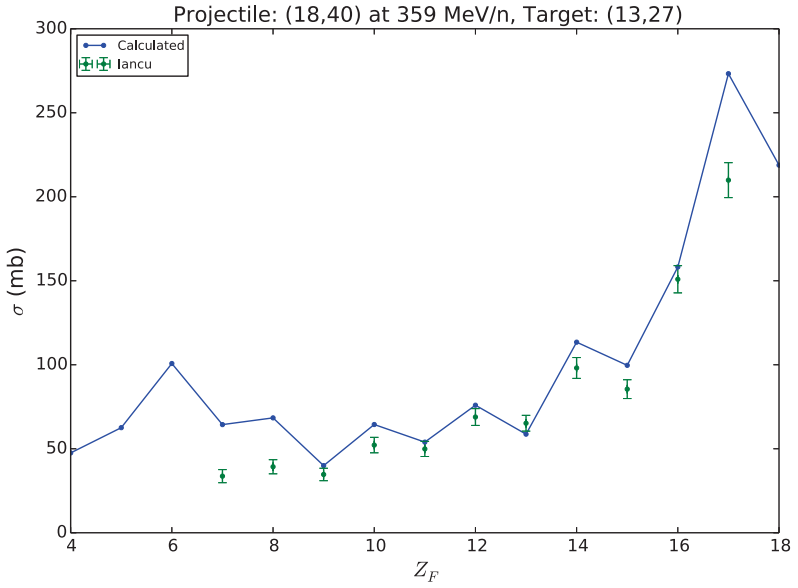


Figure 4.42: Elemental production cross sections (solid) compared with experimental measurements (error bars) from Ref. [18] for the reaction of ^{40}Ar on ^{27}Al at 359 MeV/A.

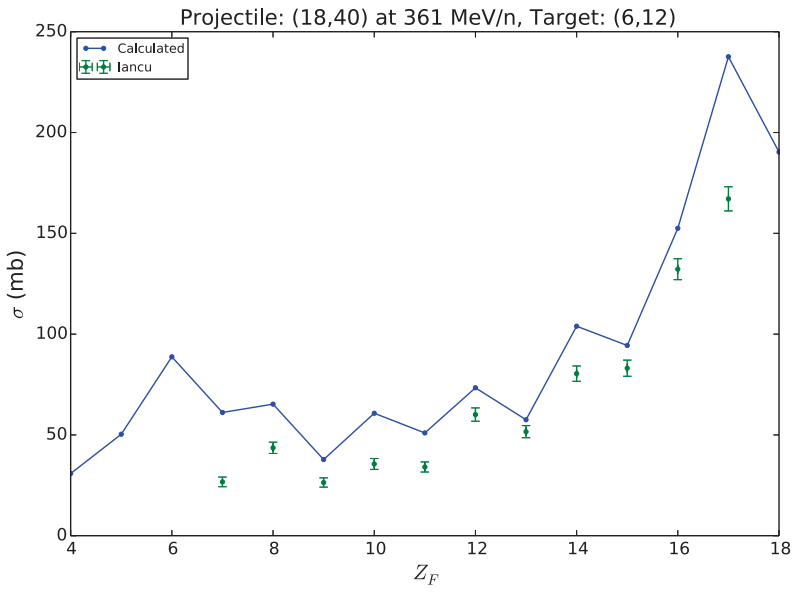


Figure 4.43: Elemental production cross sections (solid) compared with experimental measurements (error bars) from Ref. [18] for the reaction of ^{40}Ar on ^{12}C at 361 MeV/A.

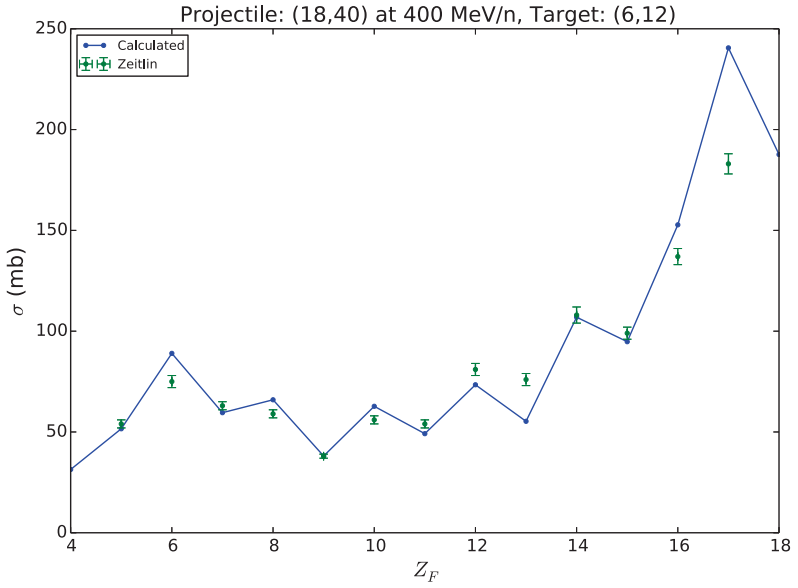


Figure 4.44: Elemental production cross sections (solid) compared with experimental measurements (error bars) from Ref. [54] for the reaction of ^{40}Ar on ^{12}C at 400 MeV/A.

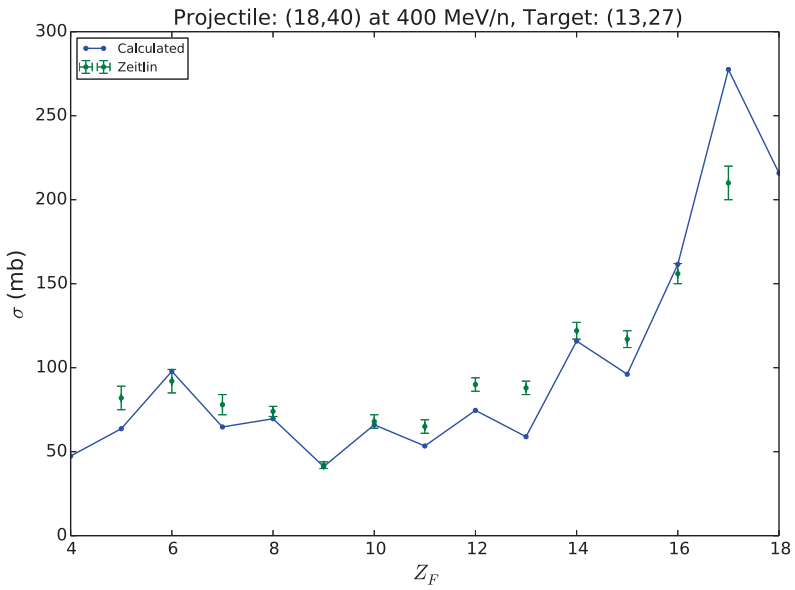


Figure 4.45: Elemental production cross sections (solid) compared with experimental measurements (error bars) from Ref. [54] for the reaction of ^{40}Ar on ^{27}Al at 400 MeV/A.

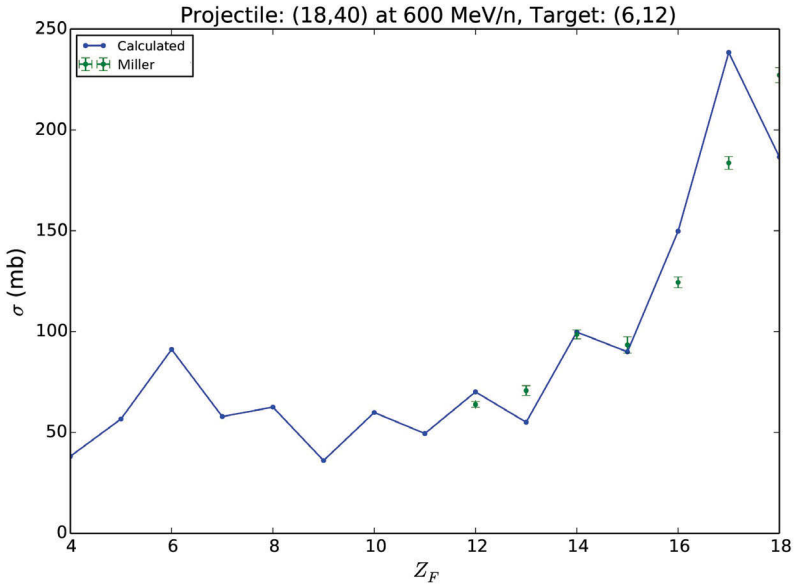


Figure 4.46: Elemental production cross sections (solid) compared with experimental measurements (error bars) from Ref. [29] for the reaction of ^{40}Ar on ^{12}C at 600 MeV/A.

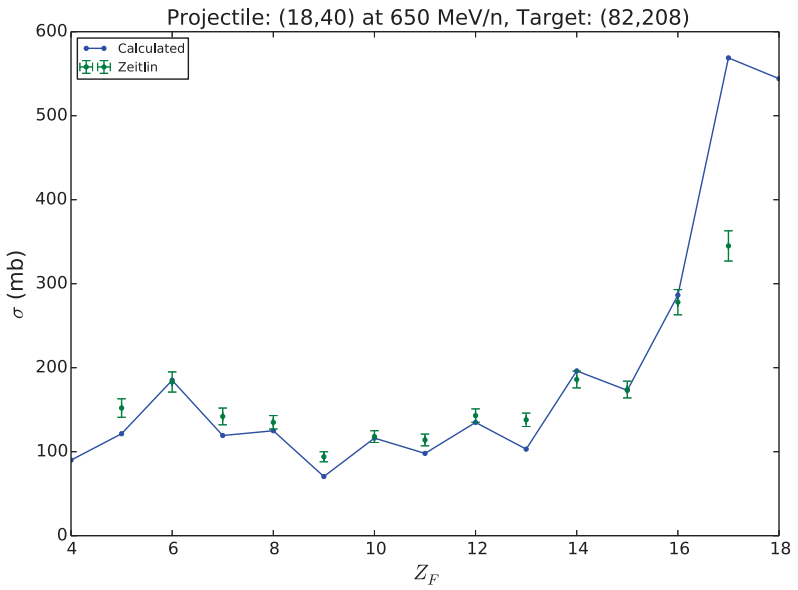


Figure 4.47: Elemental production cross sections (solid) compared with experimental measurements (error bars) from Ref. [54] for the reaction of ^{40}Ar on ^{208}Pb at 650 MeV/A.

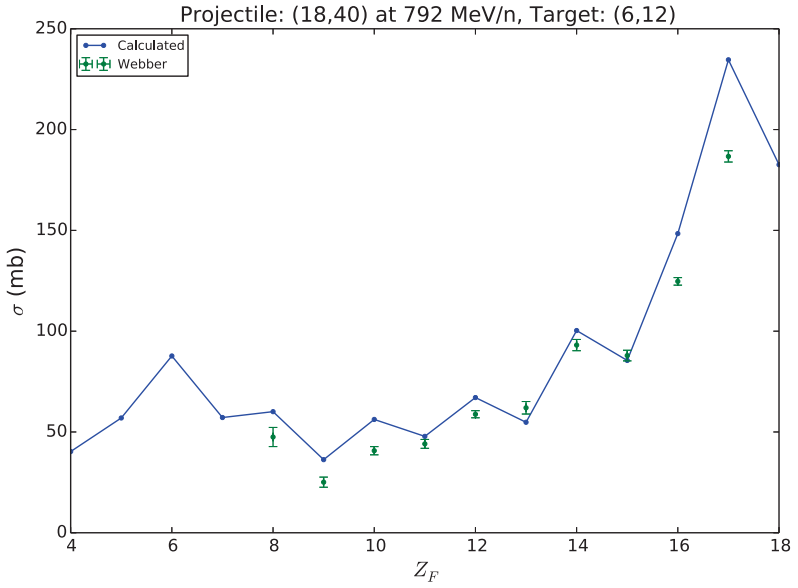


Figure 4.48: Elemental production cross sections (solid) compared with experimental measurements (error bars) from Ref. [48] for the reaction of ^{40}Ar on ^{12}C at 792 MeV/A.

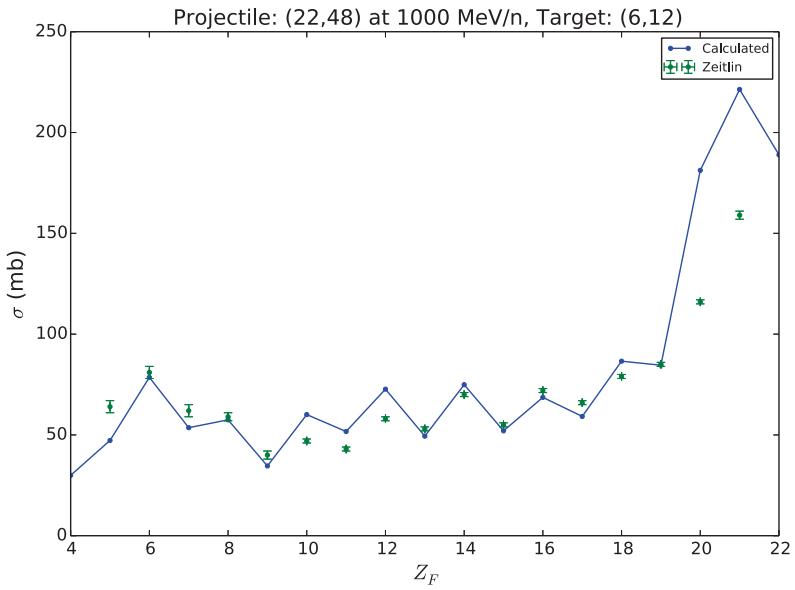


Figure 4.49: Elemental production cross sections (solid) compared with experimental measurements (error bars) from Ref. [54] for the reaction of ^{48}Ti on ^{12}C at 1000 MeV/A.

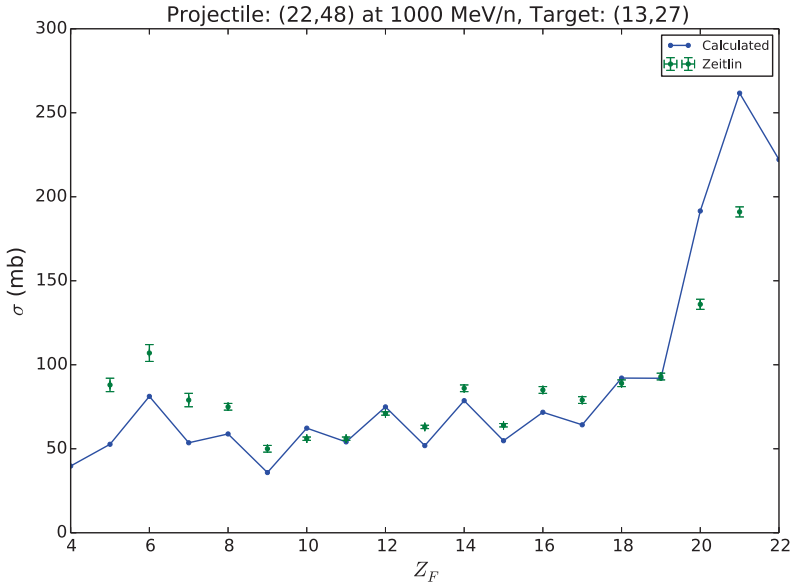


Figure 4.50: Elemental production cross sections (solid) compared with experimental measurements (error bars) from Ref. [54] for the reaction of ^{48}Ti on ^{27}Al at 1000 MeV/A.

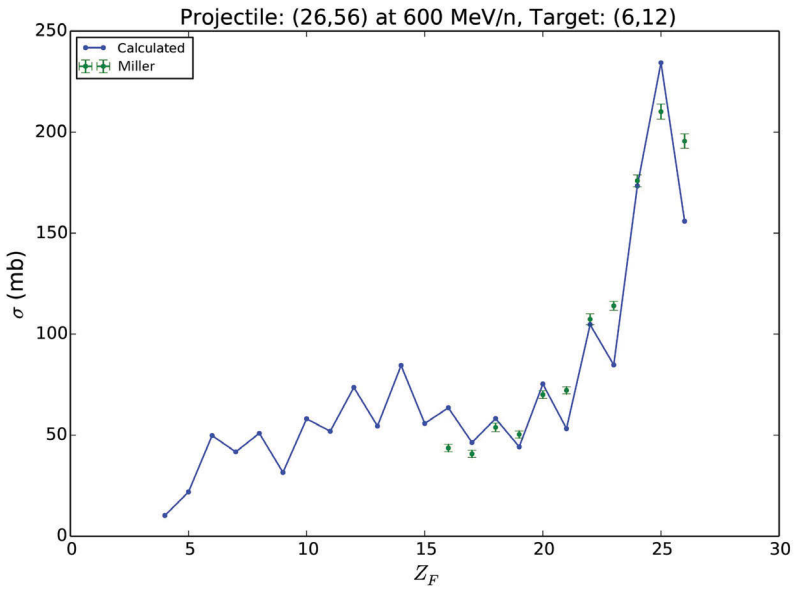


Figure 4.51: Elemental production cross sections (solid) compared with experimental measurements (error bars) from Ref. [29] for the reaction of ^{56}Fe on ^{12}C at 600 MeV/A.

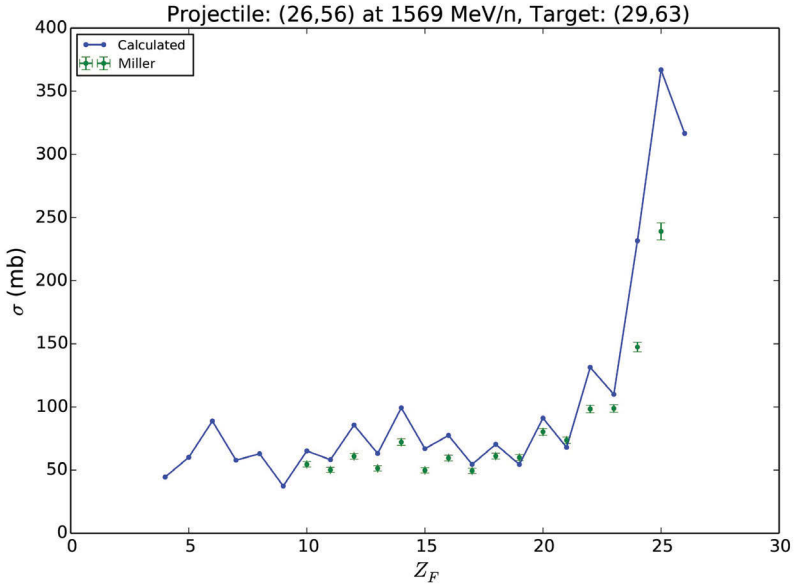


Figure 4.52: Elemental production cross sections (solid) compared with experimental measurements (error bars) from Ref. [29] for the reaction of ^{56}Fe on ^{63}Cu at 1569 MeV/A.

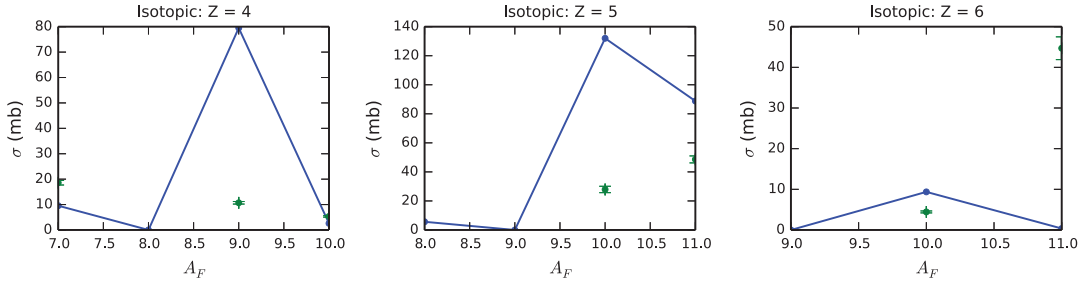


Figure 4.53: Isotopic production cross sections (solid) compared with experimental measurements (error bars) from Ref. [29] for the reaction of ^{12}C on ^{12}C at 1050 MeV/A.

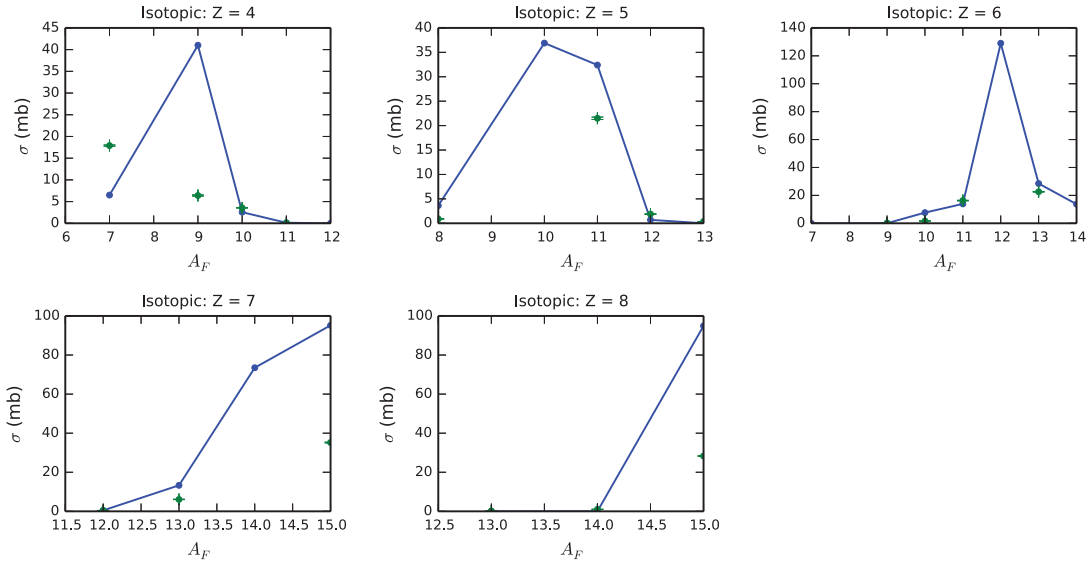


Figure 4.54: Isotopic production cross sections (solid) compared with experimental measurements (error bars) from Ref. [55] for the reaction of ^{16}O on ^{12}C at 290 MeV/A.

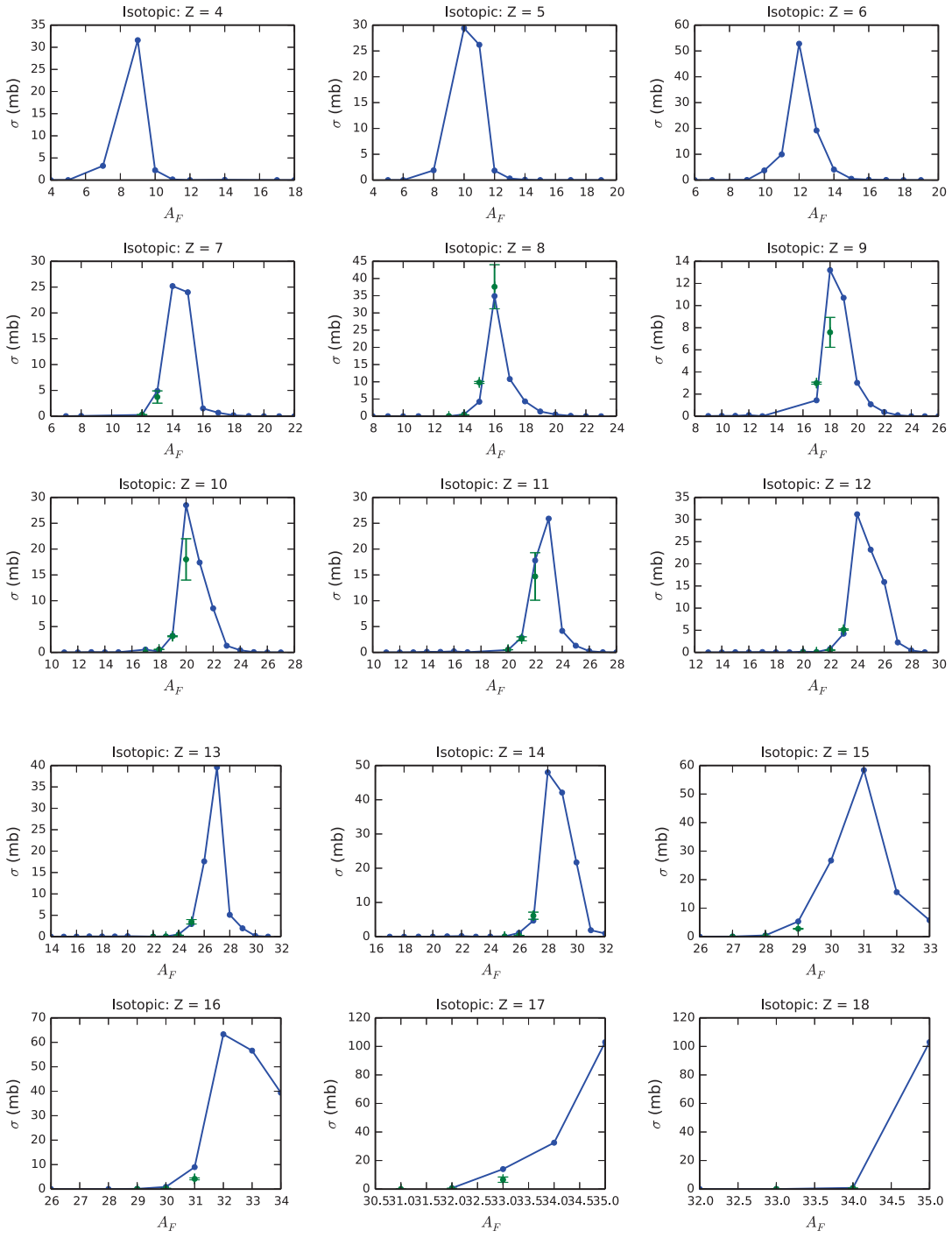


Figure 4.55: Isotopic production cross sections (solid) compared with experimental measurements (error bars) from Ref. [7] for the reaction of ^{36}Ar on ^{9}Be at 1050 MeV/A.

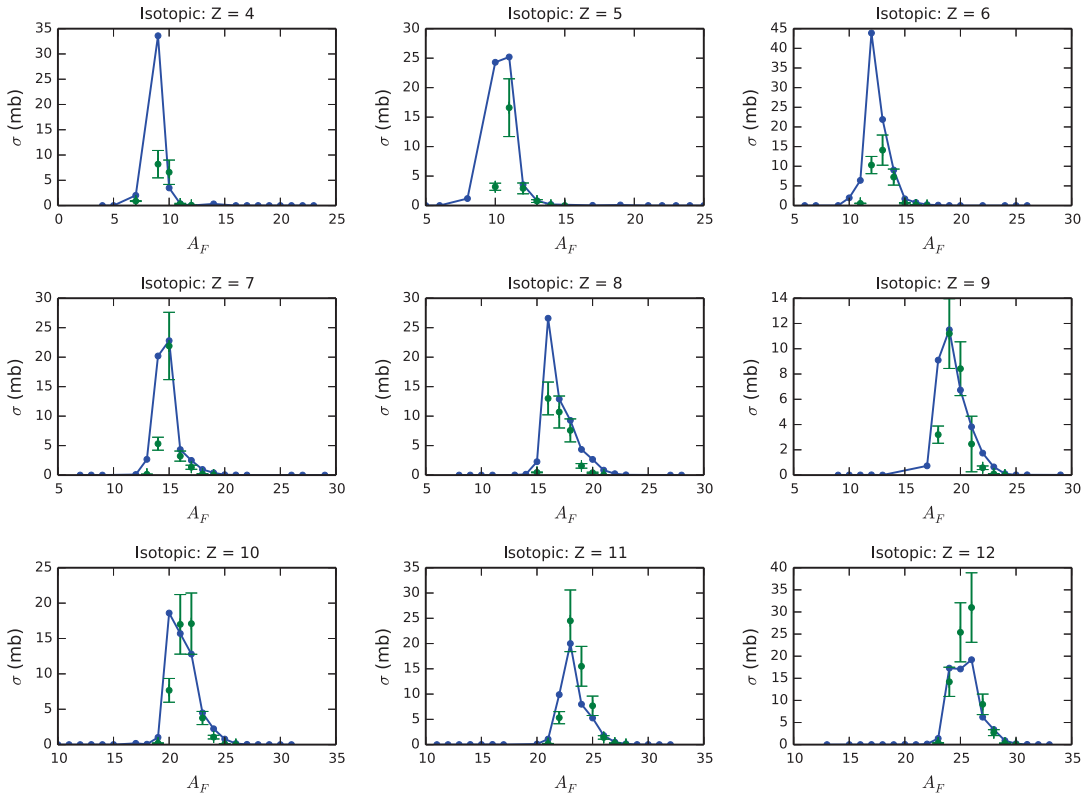


Figure 4.56: Isotopic production cross sections (solid) compared with experimental measurements (error bars) from Ref. [31] for the reaction of ^{40}Ar on ^{9}Be at 90 MeV/A.

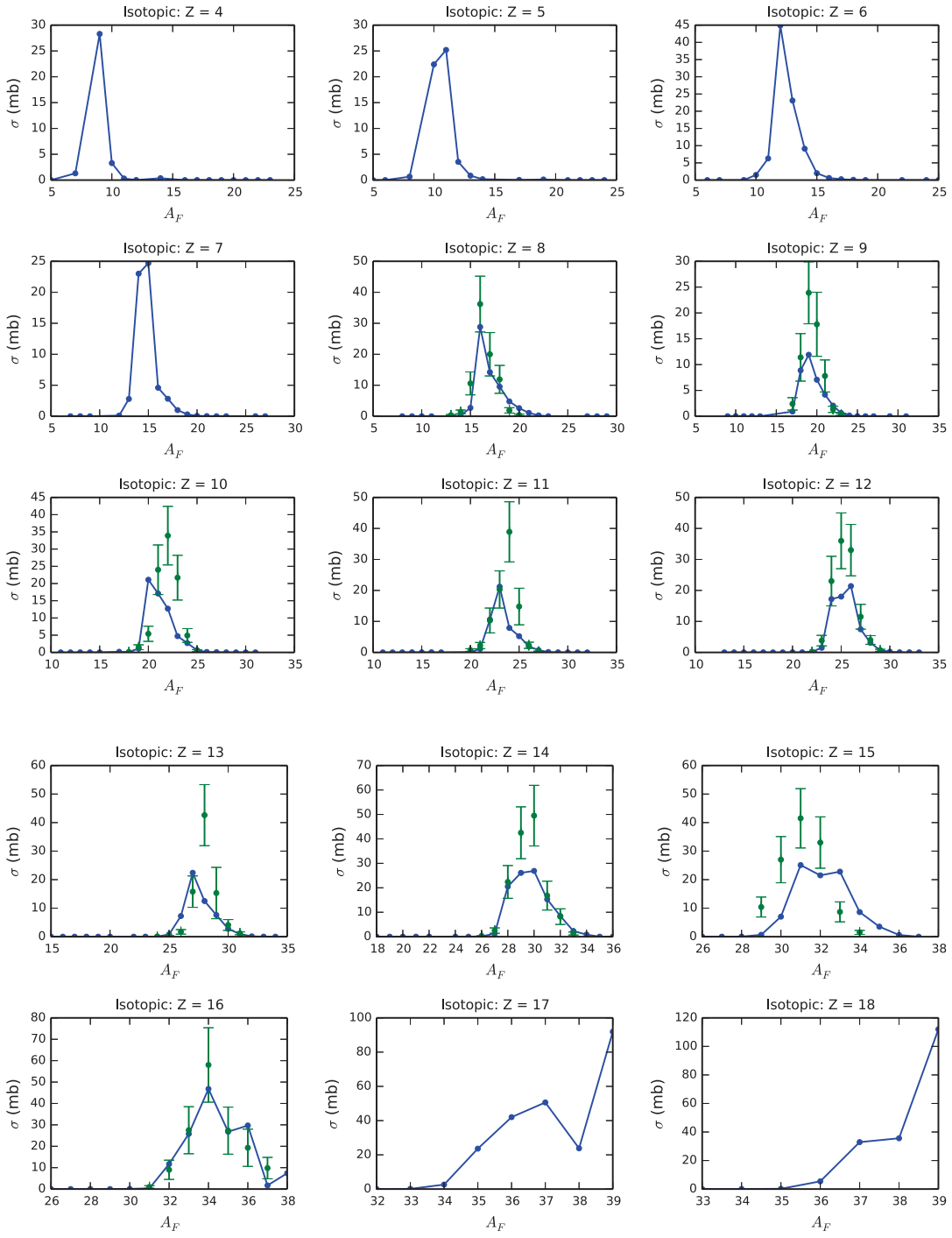


Figure 4.57: Isotopic production cross sections (solid) compared with experimental measurements (error bars) from Ref. [47] for the reaction of ^{40}Ar on ^{12}C at 213 MeV/A.

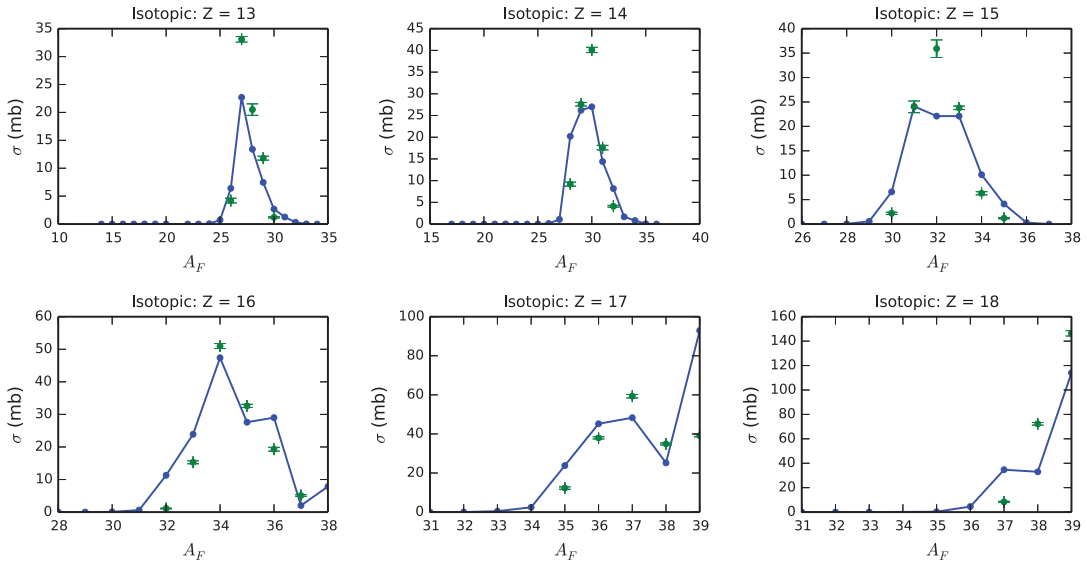


Figure 4.58: Isotopic production cross sections (solid) compared with experimental measurements (error bars) from Ref. [29] for the reaction of ^{40}Ar on ^{12}C at 600 MeV/A.

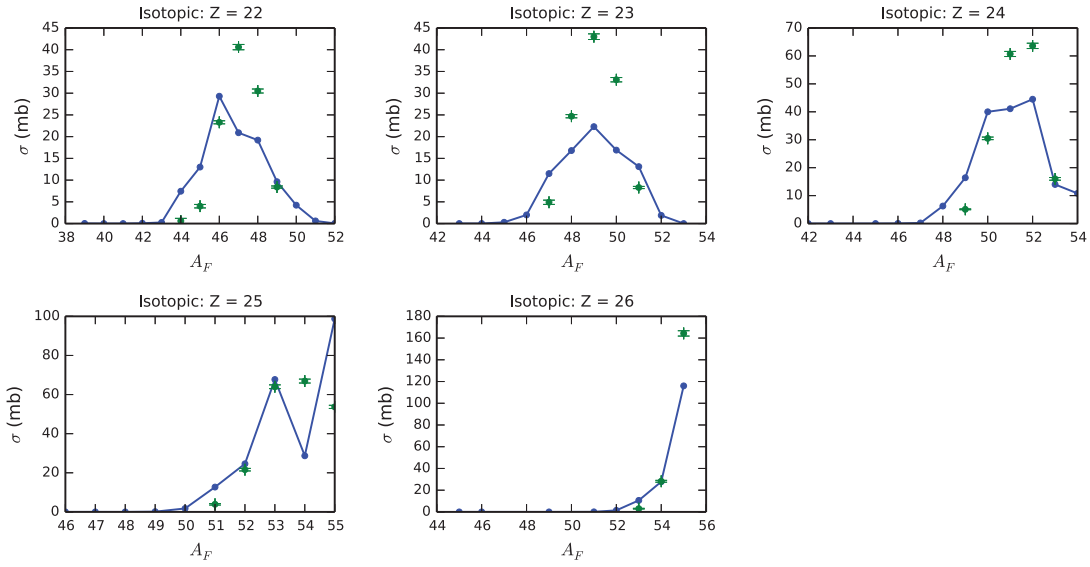


Figure 4.59: Isotopic production cross sections (solid) compared with experimental measurements (error bars) from Ref. [29] for the reaction of ^{56}Fe on ^{12}C at 600 MeV/A.

4.4 Conclusion

The RAADFRG nuclear fragmentation code has been developed to predict total fragmentation production yields for collisions of heavy charged nuclei at intermediate to high energies. The model has been developed for space radiation applications with particular interest placed on light ion production. In this formalism, there three individual light ion production mechanisms. The first mechanism is electromagnetic dissociation from the parent nucleus, in which there is no physical overlap of the projectile and target. The second and third mechanisms are coupled.

This code follows the abrasion/ablation collision theory in which the reaction is assumed to occur in two stages. In the first stage, nucleons within the overlap region between the two nuclei are sheared from their parent nucleus. These abraded nucleons may deposit energy into the remaining pre-fragment nucleus in this process. Nucleons with similar momenta will coalesce, forming a light ion. The coalescence model detailed in this manuscript assumes that particles occupying a spherical coalescence volume in momentum space will bind together. The radius of this volume is given as a parameterization. This parameterization sufficiently reproduces light ion cross sections for all combinations of projectile/target/energies studied. However, further investigation of the performance for low energy reactions is recommended.

The second stage is pre-fragment deexcitation via light ion emission. The remaining portion of the projectile nucleus has some amount of excitation energy after the abrasion process. Depending on the amount of excitation energy, a pre-fragment nucleus may emit several light particles in order to reach ground state. The emission process is handled using the Weisskopf-Ewing formalism. A pairing energy correction is made to the exponent in the level density formula in order to reproduce the odd-even behavior present in experimental data. Inconsistencies between calculated and experimentally measured spectra indicate that the processes contributing to the excitation energy of the initial pre-fragment nucleus may need to be studied further, such as the abraded nucleon escape probability and frictional spectator energy depositions.

Bibliography

[1] Adamczyk, A. M., Norman, R. B., Sriprisan, S. I., Townsend, L. W., Norbury, J. W., Blattnig, S. R., and Slaba, T. S. (2012). Nucfrg3: Light ion improvements to the nuclear fragmentation model. *Nuclear Instruments and Methods in Physics Research Section A: Accelerators, Spectrometers, Detectors and Associated Equipment*, 678:21–32. 3, 9, 19, 20, 22

[2] Auble, R. L., Ball, J. B., Bertrand, F. E., Fulmer, C. B., Hensley, D. C., Lee, I. Y., Robinson, R. L., Stelson, P. H., Wong, C. Y., Hendrie, D. L., Holmgren, H. D., and Silk, J. D. (1983). Light ion emission from reactions induced by 0.8-2.4 gev ^{16}O projectiles. *Phys. Rev. C*, 28:1552–1564. 8, 9, 24

[3] Awes, T. C., Poggi, G., Gelbke, C. K., Back, B. B., Glagola, B. G., Breuer, H., and Viola, V. E. (1981). Precompound emission of light particles in the reaction ^{16}O+^{238}U at 20 mev/nucleon. *Phys. Rev. C*, 24:89–110. 8, 9, 19, 24

[4] Beach, M. (2014). *Light-Ion Production From Intermediate-Energy Heavy-Ion Interactions*. PhD thesis, University of Tennessee Knoxville. 10, 24

[5] Behkami, A. N., Kargar, Z., and Nasrabadi, N. (2002). Level density parameter study using a microscopic model. *Phys. Rev. C*, 66:064307. 7

[6] Bethe, H. A. and Bacher, R. F. (1936). Nuclear physics a. stationary states of nuclei. *Rev. Mod. Phys.*, 8:82–229. 13

[7] Caamao, M., Cortina-Gil, D., Smmerer, K., Benlliure, J., Casarejos, E., Geissel, H., Mnzenberg, G., and Pereira, J. (2004). Production cross-sections and momentum distributions of fragments from neutron-deficient ^{36}Ar at 1.05 a gev. *Nuclear Physics, Section A*, 733(3):187–199. xiii, 56

[8] Cucinotta, F. A. (2010). Radiation risk acceptability and limitations. 2

[9] Dostrovsky, I., Fraenkel, Z., and Friedlander, G. (1959). Monte carlo calculations of nuclear evaporation processes. iii. applications to low-energy reactions. *Phys. Rev.*, 116:683–702. vii, 6, 13, 15, 16, 70

[10] Gaimard, J.-J. and Schmidt, K.-H. (1991). A reexamination of the abrasion-ablation model for the description of the nuclear fragmentation reaction. *Nuclear Physics A*, 531(3):709 – 745. 8

[11] Gilbert, A. and Cameron, A. G. W. (1965). A composite nuclear-level density formula with shell corrections. *Canadian Journal of Physics*, 43(8):1446–1496. 7

[12] Goldhaber, A. (1974). Statistical models of fragmentation processes. *Physics Letters B*, 53(4):306 – 308. 21

[13] Gosset, J., Gutbrod, H. H., Meyer, W. G., Poskanzer, A. M., Sandoval, A., Stock, R., and Westfall, G. D. (1977). Central collisions of relativistic heavy ions. *Phys. Rev. C*, 16:629–657. 9

[14] Greco, V., Ko, C. M., and Lévai, P. (2003). Partonic coalescence in relativistic heavy ion collisions. *Phys. Rev. C*, 68:034904. 8

[15] Greiner, D. E., Lindstrom, P. J., Heckman, H. H., Cork, B., and Bieser, F. S. (1975). Momentum distributions of isotopes produced by fragmentation of relativistic ^{12}C and ^{16}O projectiles. *Phys. Rev. Lett.*, 35:152–155. 21

[16] Gutbrod, H. H., Sandoval, A., Johansen, P. J., Poskanzer, A. M., Gosset, J., Meyer, W. G., Westfall, G. D., and Stock, R. (1976). Final-state interactions in the production of hydrogen and helium isotopes by relativistic heavy ions on uranium. *Phys. Rev. Lett.*, 37:667–670. 9

[17] Hurwitz, H. and Bethe, H. A. (1951). Neutron capture cross sections and level density. *Phys. Rev.*, 81:898–898. 6, 15, 16

[18] Iancu, G., Flesch, F., and Heinrich, W. (2005). Nuclear fragmentation cross-sections of 400 a mev ^{36}Ar and ^{40}Ar in collisions with light and heavy target nuclei. *Radiation Measurements*, 39(5):525–533. xi, xii, 45, 46, 49, 50

[19] Kataria, S. (1985). Deformation and shell-dependent nuclear level-density formula. *Nuclear Physics A*, 437(2):397 – 406. 7

[20] Khan, F., Khandelwal, G. S., Townsend, L. W., Wilson, J. W., and Norbury, J. W. (1991). Optical model description of momentum transfer in relativistic heavy ion collisions. *Phys. Rev. C*, 43:1372–1377. 21

[21] Khan, F. and Townsend, L. W. (1993). Widths of transverse momentum distributions in intermediate-energy heavy-ion collisions. *Phys. Rev. C*, 48:R513–R516. 21

[22] Khan, F., Townsend, L. W., Tripathi, R. K., and Cucinotta, F. A. (1993). Universal characteristics of transverse momentum transfer in intermediate energy heavy ion collisions. *Phys. Rev. C*, 48:926–928. 21

[23] Kolybasov, V. and Sokolskikh, Y. (1992). On the graph approach to the coalescence model. *Physics Letters B*, 276(4):409 – 412. 10

[24] Lang, J. M. B. and Couteur, K. J. L. (1954). Statistics of nuclear levels. *Proceedings of the Physical Society. Section A*, 67(7):586. 7

[25] Lemaire, M.-C., Nagamiya, S., Schnetzer, S., Steiner, H., and Tanihata, I. (1979). Composite particle emission in relativistic heavy ion collisions. *Physics Letters B*, 85(1):38 – 42. 10, 24

[26] Lin, Z.-W. (2007). Determination of important nuclear fragmentation processes for human space radiation protection. *Phys. Rev. C*, 75:034609. 3

[27] Lindstrom, P. J., Greiner, D. E., Heckman, H. H., Cork, B., and Bieser, F. S. (1975). Isotope production cross sections from the fragmentation of ^{16}O and ^{12}C at relativistic energies. lbnl paper lbl-3650. 24

[28] Mashnik, S. G., Kerby, L. M., Gudima, K. K., Sierk, A. J., Bull, J. S., and James, M. R. (2017). Production of energetic light fragments in extensions of the cem and laqgsm event generators of the monte carlo transport code mcnp6. *Phys. Rev. C*, 95:034613. 8, 24

[29] Miller, J., Cucinotta, F. A., Shinn, J. L., Tripathi, R. K., Badavi, F. F., Chun, S. Y., Heilbronn, L., Norbury, J. W., Wilson, J. W., and Zeitlin, C. J. (1995). Nucfrg2: An

evaluation of the semiempirical nuclear fragmentation database - nasa-tp-3533. Technical report. ix, x, xii, xiii, xiv, 35, 36, 37, 38, 51, 54, 55, 59

[30] Moller, P. and Nix, J. (1992). Nuclear pairing models. *Nuclear Physics A*, 536(1):20 – 60. 7

[31] Momota, S., Notani, M., Ito, S., Ozawa, A., Suzuki, T., Tanihata, I., Aoi, N., Sakurai, H., Teranishi, T., Watanabe, Y., Yoshida, A., Inabe, A., Kubo, T., Okuno, H., Fukuda, N., Iwasaki, H., Yoneda, K., Ogawa, H., Kitagawa, A., Kanazawa, M., Torikoshi, M., Suda, M., and Ono, A. (2002). Production of projectile-like fragments at intermediate energies. *Nuclear Physics, Section A*, 701(1):150–155. xi, xiii, 46, 57

[32] Morrissey, D. J., Oliveira, L. F., Rasmussen, J. O., Seaborg, G. T., Yariv, Y., and Fraenkel, Z. (1979). Microscopic and macroscopic model calculations of relativistic heavy-ion fragmentation reactions. *Phys. Rev. Lett.*, 43:1139–1142. 13

[33] Nagamiya, S., Lemaire, M. C., Moeller, E., Schnetzer, S., Shapiro, G., Steiner, H., and Tanihata, I. (1981). Production of pions and light fragments at large angles in high-energy nuclear collisions. *Phys. Rev. C*, 24:971–1009. 8, 24

[34] Nakai, K., Terasaki, O., Shibata, T. A., En'yo, H., and Arai, I. (1982). Composite particle production in high-energy reactions and size of production source. *Phys. Rev. C*, 25:1992–1995. 10

[35] Norbury, J. W. and Adamczyk, A. (2007). Differential cross sections for electromagnetic dissociation. *Nuclear Instruments and Methods in Physics Research Section B: Beam Interactions with Materials and Atoms*, 254(2):177–181. 25

[36] Norbury, J. W. and Slaba, T. C. (2014). Space radiation accelerator experiments - the role of neutrons and light ions. *Life Sciences in Space Research*, 3:90 – 94. 2

[37] Oliveira, L. F., Donangelo, R., and Rasmussen, J. O. (1979). Abrasion-ablation calculations of large fragment yields from relativistic heavy ion reactions. *Phys. Rev. C*, 19:826–833. 13

[38] Olson, D. L., Berman, B. L., Greiner, D. E., Heckman, H. H., Lindstrom, P. J., and Crawford, H. J. (1983). Factorization of fragment-production cross sections in relativistic heavy-ion collisions. *Phys. Rev. C*, 28:1602–1613. viii, ix, 30, 31, 32, 33

[39] PourArsalan, M. (2012). *Secondary Light Particle Data Base Development Using a Thermodynamic Coalescence Model*. PhD thesis, University of Tennessee Knoxville. 10, 24

[40] Shlomo, S. and Natowitz, J. B. (1991). Temperature and mass dependence of level density parameter. *Phys. Rev. C*, 44:2878–2880. 7

[41] Townsend, L., Cucinotta, F., and Heilbronn, L. (2002). Nuclear model calculations and their role in space radiation research. *Advances in Space Research*, 30(4):907 – 916. 12, 13

[42] Townsend, L., Ramsey, C., Tripathi, R., Cucinotta, F., and Norbury, J. (1999). Optical model methods of predicting nuclide production cross sections from heavy ion fragmentation. *Nuclear Instruments and Methods in Physics Research Section B: Beam Interactions with Materials and Atoms*, 149(4):401 – 413. 12

[43] Townsend, L. W., Khan, F., and Tripathi, R. K. (1993). Optical model analyses of 1.65a gev argon fragmentation: Cross sections and momentum distributions. *Phys. Rev. C*, 48:2912–2919. 21

[44] Tripathi, R., Cucinotta, F., and Wilson, J. (1999). Medium modified nucleon-nucleon cross sections in a nucleus. *Nuclear Instruments and Methods in Physics Research Section B: Beam Interactions with Materials and Atoms*, 152(4):425 – 431. 12

[45] Tripathi, R. K. and Townsend, L. W. (1994). Simple parametrization of fragment reduced widths in heavy ion collisions. *Phys. Rev. C*, 49:2237–2239. 21

[46] Tripathi, R. K., Townsend, L. W., and Khan, F. (1994). Role of intrinsic width in fragment momentum distributions in heavy ion collisions. *Phys. Rev. C*, 49:R1775–R1777. 21

[47] Viyogi, Y., Symons, T., Doll, P., Greiner, D., Heckman, H., Hendrie, D., Lindstrom, P., Mahoney, J., Scott, D., Van Bibber, K., Westfall, G., Wieman, H., Crawford, H., McParland, C., Gelbke, C., Viyogi, C., and Doll, C. (1979). Fragmentations of ^{40}Ar at 213 mev/nucleon. *Physical Review Letters*, 42(1):33–36. xi, xiii, 47, 58

[48] Webber, W. R., Kish, J. C., and Schrier, D. A. (1990). Individual isotopic fragmentation cross sections of relativistic nuclei in hydrogen, helium, and carbon targets. *Phys. Rev. C*, 41:547–565. xii, 52

[49] Weisskopf, V. (1937). Statistics and nuclear reactions. *Phys. Rev.*, 52:295–303. 15

[50] Weisskopf, V. F. and Ewing, D. H. (1940). On the yield of nuclear reactions with heavy elements. *Phys. Rev.*, 57:472–485. 6, 14

[51] Weizsäcker, C. F. v. (1935). Zur theorie der kernmassen. *Zeitschrift für Physik*, 96(7):431–458. 13

[52] Zeitlin, C., Fukumura, A., Guetersloh, S., Heilbronn, L., Iwata, Y., Miller, J., and Murakami, T. (2007). Fragmentation cross sections of ^{28}Si at beam energies from 290 a to 1200 a mev. *Nuclear Physics, Section A*, 784(1):341–367. x, 38, 39, 40

[53] Zeitlin, C., Guetersloh, S., Heilbronn, L., Miller, J., Fukumura, A., Iwata, Y., and Murakami, T. (2008a). Fragmentation cross sections of 290 and 400 mev/nucleon ^{12}C beams on elemental targets. ix, 35

[54] Zeitlin, C., Guetersloh, S., Heilbronn, L., Miller, J., Fukumura, A., Iwata, Y., Murakami, T., Sihver, L., and Mancusi, D. (2008b). Fragmentation cross sections of medium-energy ^{35}Cl, ^{40}Ar, and ^{48}Ti beams on elemental targets. x, xi, xii, xiii, 40, 41, 42, 43, 44, 45, 47, 48, 49, 50, 51, 52, 53

[55] Zeitlin, C., Miller, J., Guetersloh, S., Heilbronn, L., Fukumura, A., Iwata, Y., Murakami, T., Blattnig, S., Norman, R., and Mashnik, S. (2011). Fragmentation of ^{14}N, ^{16}O, ^{20}Ne, and ^{24}Mg nuclei at 290 to 1000 mev/nucleon. *Physical Review C - Nuclear Physics*, 83(3). ix, xiii, 36, 37, 55

Appendices

Appendix A

Relevant Tables

Table A.1: Tabulated parameters for calculating charged particle Coulomb barrier (k_j), and capture cross sections (c_j) Ref. [9]. See Section 3.3.3 for implementation.

Z_D	$k_{j=2}$	$k_{j=3}$	$k_{j=4}$	$k_{j=5}$	$k_{j=6}$	$c_{j=2}$	$c_{j=3}$	$c_{j=4}$	$c_{j=5}$	$c_{j=6}$
10	0.420	0.480	0.540	0.620	0.680	0.50000	0.25000	0.16700	0.13333	0.10000
20	0.580	0.640	0.700	0.760	0.820	0.28000	0.14000	0.09300	0.13333	0.10000
30	0.680	0.740	0.800	0.850	0.910	0.20000	0.10000	0.06770	0.13333	0.10000
40	0.725	0.785	0.845	0.880	0.940	0.17500	0.08750	0.05830	0.12000	0.09000
50	0.770	0.830	0.890	0.910	0.970	0.15000	0.07500	0.05000	0.10660	0.08000
60	0.785	0.845	0.905	0.915	0.975	0.12500	0.06250	0.04750	0.09350	0.07000
≥ 70	0.800	0.860	0.920	0.920	0.980	0.10000	0.05000	0.03333	0.08010	0.06000

Vita

Wouter de Wet was born in Vereeniging, South Africa to parents Johannes and Santie. Wouter spent the majority of his childhood in Chattanooga, TN as the middle child of three boys. He graduated from Signal Mountain High School in 2010 and continued on to earn three degrees in Nuclear Engineering at the University of Tennessee, Knoxville. He completed his Bachelor's Degree in 2014, Master's in 2015, and his Doctorate in 2017. Wouter is happily married to Lauren. They have two dogs, Max and Copper.